The KBSS–KCWI survey: the connection between extended Ly α haloes and galaxy azimuthal angle at $z \sim$ 2–3

Yuguang Chen, (陈昱光) [1]*, Charles C. Steidel [1], Dawn K. Erb [2], David R. Law [3], Ryan F. Trainor [4], Naveen A. Reddy [5], Alice E. Shapley [6], Anthony J. Pahl [6], Allison L. Strom [7], Noah R. Lamb [8], Zhihui Li, (李智慧) [1] and Gwen C. Rudie [9]

[1]*Cahill Center for Astronomy and Astrophysics, California Institute of Technology, 1200 E California Blvd, MC249-17, Pasadena, CA 91125, USA*
[2]*Center for Gravitation, Cosmology, and Astrophysics, Department of Physics, University of Wisconsin-Milwaukee, 3135 N. Maryland Avenue, Milwaukee, WI 53211, USA*
[3]*Space Telescope Science Institute, 3700 San Martin Drive, Baltimore, MD 21218, USA*
[4]*Department of Physics and Astronomy, Franklin & Marshall College, 637 College Avenue, Lancaster, PA 17603, USA*
[5]*Department of Physics and Astronomy, University of California, Riverside, 900 University Avenue, Riverside, CA 92521, USA*
[6]*Department of Physics and Astronomy, University of California, Los Angeles, 430 Portola Plaza, Los Angeles, CA 90095, USA*
[7]*Department of Astrophysical Sciences, 4 Ivy Lane, Princeton University, Princeton, NJ 08544, USA*
[8]*Department of Physics, Drexel University, 32 S. 32nd Street, Philadelphia, PA 19104, USA*
[9]*The Observatories of the Carnegie Institution for Science, 813 Santa Barbara Street, Pasadena, CA 91101, USA*

ABSTRACT
We present the first statistical analysis of kinematically resolved, spatially extended Lyα emission around $z = 2$–3 galaxies in the Keck Baryonic Structure Survey (KBSS) using the Keck Cosmic Web Imager (KCWI). Our sample of 59 star-forming galaxies ($z_{med} = 2.29$) comprises the subset with typical KCWI integration times of ∼5 h and with existing imaging data from the *Hubble Space Telescope* and/or adaptive optics-assisted integral field spectroscopy. The high-resolution images were used to evaluate the azimuthal dependence of the diffuse Lyα emission with respect to the stellar continuum within projected galactocentric distances of ≲30 proper kpc. We introduce cylindrically projected 2D spectra (CP2D) that map the averaged Lyα spectral profile over a specified range of azimuthal angle, as a function of impact parameter around galaxies. The averaged CP2D spectrum of all galaxies shows clear signatures of Lyα resonant scattering by outflowing gas. We stacked the CP2D spectra of individual galaxies over ranges of azimuthal angle with respect to their major axes. The extended Lyα emission along the galaxy principal axes is statistically indistinguishable, with residual asymmetry of ≤2 per cent (∼2σ) of the integrated Lyα emission. The symmetry implies that the Lyα scattering medium is dominated by outflows in all directions within 30 kpc. Meanwhile, we find that the blueshifted component of Lyα emission is marginally stronger along galaxy minor axes for galaxies with relatively weak Lyα emission. We speculate that this weak directional dependence of Lyα emission becomes discernible only when the Lyα escape fraction is low. These discoveries highlight the need for similar analyses in simulations with Lyα radiative transfer modelling.

Key words: galaxies: evolution – galaxies: high-redshift – galaxies: ISM.

1 INTRODUCTION

Extended 'haloes' of diffuse Lyman-alpha (Ly α) emission, extending to many times larger radii than starlight, are nearly ubiquitous around rapidly star-forming galaxies at redshift $z > 2$ (e.g. Steidel et al. 2011; Wisotzki et al. 2016; Leclercq et al. 2017; Wisotzki et al. 2018). While there is not yet consensus on the dominant physical mechanism giving rise to diffuse Lyα haloes, there is general agreement on the list of potential sources, all of which depend on substantial cool hydrogen gas in the circumgalactic medium (CGM; e.g. Ouchi, Ono & Shibuya 2020): (1) resonant scattering of Lyα produced by recombination of gas photoionized by massive stars or active galactic nuclei (AGNs), i.e. a central source, where

Lyα photons are subsequently scattered until they find optically thin channels to escape; (2) *in situ* photoionization of H I by the metagalactic ultraviolet (UV) ionizing radiation field combined with local sources and followed by recombination (sometimes called 'fluorescence'); (3) accreting gas losing energy via collisional excitation of Lyα (sometimes referred to as 'gravitational cooling'); and (4) emission from unresolved satellite galaxies in the haloes of larger central galaxies. In principle, the observed surface brightness (SB), spatial distribution, and kinematics of Lyα emission can discriminate between the various mechanisms and, perhaps more importantly, can provide direct information on the degree to which gas in the CGM is accreting, outflowing, or quiescent. Lyα emission from the CGM, if interpreted correctly, can provide a detailed map of the cool component of the dominant baryon reservoir associated with forming galaxies, as well as constraints on large-scale gas flows that are an essential part of the current galaxy formation paradigm.

* E-mail: yuguangchen@astro.caltech.edu

Because a Lyα photon is produced by nearly every photoionization of hydrogen, the intrinsic Lyα luminosity of a rapidly star-forming galaxy can be very high and thus easily detected (Partridge & Peebles 1967). However, due to its very high transition probability, Lyα is resonantly scattered until the last scattering event gives it an emitted frequency and direction such that the optical depth remains low along a trajectory that allows it to escape from the host galaxy. When the Lyα optical depth is high in all directions, the vastly increased effective path length – due to large numbers of scattering events during the time the photon is radiatively trapped – increases the probability that the photon is destroyed by dust or emitted via two-photon mechanism. But Lyα photons that are not absorbed by dust grains or converted to two-photon radiation must eventually escape, with the final scattering resulting in the photon having a frequency and direction such that the photon can freely stream without further interaction with a hydrogen atom. The radiative transfer of Lyα thus depends in a complex way on the distribution, clumpiness, and kinematics of H I within the host galaxy, as well as on where and how the photon was produced initially. But the added complexity is counter-balanced by the availability of a great deal of information about the scattering medium itself that is otherwise difficult or impossible to observe directly: i.e. the neutral hydrogen distribution and kinematics in the CGM.

Since the commissioning of sensitive integral-field spectrometers on large ground-based telescopes – the Multi Unit Spectroscopic Explorer (MUSE; Bacon et al. 2010) on the Very Large Telescopes (VLT) of the European Southern Observatory and the Keck Cosmic Web Imager (KCWI; Morrissey et al. 2018) at the Keck Observatory – it has become possible to routinely detect diffuse Lyα emission haloes around individual galaxies at high redshift (e.g. Wisotzki et al. 2016; Leclercq et al. 2017) and to simultaneously measure the spatially resolved Lyα kinematics (e.g. Erb, Steidel & Chen 2018; Claeyssens et al. 2019; Leclercq et al. 2020). Such observations can then be interpreted in terms of simple expectations based on Lyα radiative transfer; for example, a generic expectation is that most Lyα emission involving scattered photons (i.e. those that must pass through an H I gas distribution before escaping their host) will exhibit a 'double-peaked' spectral profile, where the relative strength of the blueshifted and redshifted peaks may be modulated by the net velocity field of the emitting gas. In the idealized case of a spherical shell of outflowing (infalling) gas, one predicts that an external observer will measure a dominant red (blue) peak (Verhamme, Schaerer & Maselli 2006). The fact that most (∼90 per cent) of star-forming galaxy 'down the barrel' (DTB) spectra with Lyα in emission in the central portions exhibit dominant red peaks (e.g. Pettini et al. 2001; Steidel et al. 2010; Kulas et al. 2012; Trainor et al. 2015; Verhamme et al. 2018; Matthee et al. 2021) has led to the conclusion that outflowing gas dominates Lyα radiative transfer, at least at small galactocentric distances.

Essentially every simulation of galaxy formation (Faucher-Giguère et al. 2010) predicts that gaseous accretion is also important – particularly at high redshifts ($z \gtrsim 2$) – and this has focused attention on systems in which a double Lyα profile with a blue-dominant peak is observed, often cited as evidence for ongoing accretion of cool gas (e.g. Martin et al. 2014, 2016; Vanzella et al. 2017; Ao et al. 2020). Quantitative predictions of Lyα emission from accreting baryons depend sensitively on the thermal state and the small-scale structure of the gas (e.g. Faucher-Giguère et al. 2010; Goerdt et al. 2010; Kollmeier et al. 2010), leading to large uncertainties in the predictions. The role played by 'local' sources of ionizing photons over and above that of the metagalactic ionizing radiation field is likely to be substantial for regions near QSOs (Cantalupo et al. 2014; Borisova et al. 2016; Cai et al. 2019; O'Sullivan et al. 2020) but

much more uncertain for star-forming galaxies, where the escape of scattered Lyα photons is much more likely than that of ionizing photons.

Models of Lyα radiative transfer have attempted to understand the dominant physics responsible for producing Lyα haloes around galaxies. Using photon-tracing algorithms with Monte Carlo simulations, Verhamme et al. (2006), Dijkstra (2014), Gronke & Dijkstra (2016), and Gronke et al. (2016) have explored the effects of resonant scattering on the emergent central Lyα line profile using various idealized H I geometries and velocity fields; in most cases, simple models can be made to fit the observed 1D profiles (Gronke 2017; Song, Seon & Hwang 2020). There have also been attempts to model or predict spatially resolved Lyα, which almost certainly depends on a galaxy's immediate environment (Zheng et al. 2011; Kakiichi & Dijkstra 2018), including both outflows and accretion flows, as well as the radiative transfer of Lyα photons from the site of initial production to escape (e.g. Faucher-Giguère et al. 2010; Lake et al. 2015; Smith et al. 2019; Byrohl et al. 2020). However, the conclusions reached as to the dominant process responsible for the extended Lyα emission have not converged, indicating that more realistic, high-resolution, cosmological zoom-in simulations may be required to capture all of the physical processes. Despite the variety of Lyα radiative transfer models to date, as far as we are aware, no specific effort has been made to statistically compare full 2D model predictions (simultaneous spatial and kinematic) to observed Lyα haloes.

Some insight into the relationship between galaxy properties and the kinematics and spatial distribution of cool gas in the CGM has been provided by studies at lower redshifts, where galaxy morphology is more easily measured. Statistical studies using absorption line probes have clearly shown that the strength of low-ionization metal lines such as Mg II, Fe II depends on where the line of sight passes through the galaxy CGM relative to the projected major axis of the galaxy – the 'azimuthal angle' (e.g. Bordoloi et al. 2011; Bouché et al. 2012; Kacprzak, Churchill & Nielsen 2012; Nielsen et al. 2015; Lan & Mo 2018; Martin et al. 2019), and the inclination of the galaxy disc relative to the line of sight (e.g. Steidel et al. 2002; Kacprzak et al. 2011). More recently, clear trends have also been observed for high ions (O VI) (Kacprzak et al. 2015). In general, these trends support a picture of star-forming galaxies in which high-velocity, collimated outflows perpendicular to the disc are responsible for the strongest absorption lines in both low and high ions, with low ions also being strong near the disc plane. Theoretically at least, accretion flows might also be quasi-collimated in the form of cold streams of gas that would tend to deposit cool gas near the disc plane (see e.g. Tumlinson, Peeples & Werk 2017). It is less clear how such a geometry for gas flows in the CGM would manifest as emission in a resonantly scattered line like Lyα. One might expect that Lyα photons would escape most readily along the minor axis, since the large velocity gradients and lower H I optical depths of outflowing material both favour Lyα escape from the host galaxy. This picture is consistent with Verhamme et al. (2012), who showed that Lyα escape is enhanced when the simulated galaxies are viewed face-on.

Observations of low-redshift, spatially resolved Lyα emission have so far been limited to small samples – e.g. in the local universe ($z < 0.2$), using the *Hubble Space Telescope* (*HST*), the 'Lyα reference sample' (LARS; Östlin et al. 2014) has obtained images probing Lyα emission around galaxies in great spatial detail, reaffirming the complex nature of Lyα radiative transfer and its relation to the host galaxies. In most cases, LARS found evidence that extended Lyα emission is most easily explained by photons produced by active star formation that then diffuse into the CGM before a last

scattering event allows escape in the observer's direction. Although there are small-scale enhancements associated with outflows, even for galaxies observed edge-on the Lyα emission is perhaps smoother than expected (Duval et al. 2016).

At $z > 2$, Lyα emission is more readily observed but detailed analyses are challenged by the relatively small galaxy sizes (both physical and angular) and the need for high spatial resolution to determine the morphology of the stellar light. In this paper, we present a statistical sample of $z > 2$ galaxies drawn from a survey using KCWI of selected regions within the Keck Baryonic Structure Survey (KBSS; Rudie et al. 2012; Steidel et al. 2014; Strom et al. 2017). Since the commissioning of KCWI in late 2017, we have obtained deep integral field unit (IFU) data (∼5-h integrations) for >100 KBSS galaxies with $z = 2$–3.5, so that the Lyα line is covered within the KCWI wavelength range; some initial results from the survey have been presented by Erb et al. (2018) and Law et al. (2018). The 59 galaxies included in our current analysis are those that, in addition to the KCWI data, have also been observed at high spatial resolution by either *HST* or adaptive optics-assisted near-IR spectroscopy using Keck/OSIRIS. The overarching goal of the study is to evaluate the spatial and spectral distribution of Lyα emission within ≃5 arcsec as compared to the principle axes defined by the galaxy morphology on smaller angular scales by each galaxy's UV/optical continuum emission. In particular, we seek to use the observed kinematics and spatial distribution of Lyα emission to evaluate whether the cool gas in the CGM of forming galaxies shows evidence for directional dependence – e.g., inflows or outflows along preferred directions – with respect to the central galaxy.

This paper is organized as follows. In Section 2, we describe the KBSS–KCWI sample; Section 3 introduces the high-resolution imaging and IFU data set; Section 4 covers the details on the measurement of the galaxy principle axes providing the definition of the galactic azimuthal angle; Section 5 presents results on the connection between Lyα haloes and galactic azimuthal angle; Section 6 looks into the connection between the Lyα azimuthal asymmetry and the overall Lyα emission properties; Section 7 checks higher-order azimuthal asymmetry of Lyα emission by dividing the sample into finer azimuthal bins; and Section 8 discusses the implications of the results, with a summary in Section 9. Throughout the paper, we assume a ΛCDM cosmology with $\Omega_m = 0.3$, $\Omega_\Lambda = 0.7$, and $h = 0.7$. Distances are given in proper units, i.e. physical kpc (pkpc).

2 THE KBSS–KCWI GALAXY SAMPLE

In late 2017, we began using the recently commissioned KCWI (Morrissey et al. 2018) on the Keck II 10-m telescope to target selected regions within the survey fields of the KBSS (Rudie et al. 2012; Steidel et al. 2014; Strom et al. 2017). The main goal of the KCWI observations has been to detect diffuse emission from the CGM (within impact parameter, $D_{\text{tran}} \lesssim 100$ pkpc) of a substantial sample of rapidly star-forming galaxies and optically faint AGN host galaxies, reaching SB sensitivity of ∼5 × 10^{-20} ergs s^{-1} cm^{-2} arcsec^{-2} (1σ) for unresolved emission lines. Such limiting SB would allow detection of the extended Lyα haloes of individual galaxies at redshifts $z \sim 2$–3 (e.g. Steidel et al. 2011) and would be capable of detecting extended diffuse UV metallic cooling line emission as predicted by simulations of galaxies with comparable mass and redshift (e.g. Sravan et al. 2016).

KCWI offers three selectable image slicer scales, each of which can be used with three different regimes of spectral resolving power, $R \equiv \lambda/\Delta\lambda$. All of the observations used in the present study were obtained using the 'medium' slicer scale and low-resolution grating

(BL), providing integral field spectra over a contiguous field of view (FoV) of 20″.3 × 16″.5 covering the common wavelength range of 3530–5530 Å with resolving power $\langle R \rangle = 1800$.

Given the relatively small solid angle of the KCWI FoV, and the total integration time desired for each pointing of ∼5 h, it was necessary to choose the KCWI pointings carefully. In general, we chose KCWI pointings to maximize the number of previously identified KBSS galaxies with $2 \lesssim z \lesssim 3.4$ within the FoV, so that the KCWI spectra would include the Lyα line as well as many other rest-frame far-UV transitions. Most of the targeted galaxies within each pointing were observed as part of KBSS in both the optical (Keck/LRIS; Oke et al. 1995; Steidel et al. 2004) and the near-IR (Keck/MOSFIRE; McLean et al. 2012; Steidel et al. 2014). The pointings were chosen so that the total sample of KBSS catalogue galaxies observed would span the full range of galaxy properties represented in the KBSS survey in terms of stellar mass (M$_*$), star formation rate (SFR), Lyα emission strength, and rest-optical nebular properties. Most of the KCWI pointings were also directed within the regions of the KBSS survey fields that have been observed at high spatial resolution by *HST*.

As of this writing, the KBSS–KCWI survey comprises 39 pointings of KCWI, including observations of 101 KBSS galaxies, of which 91 have $2 \leq z \leq 3.4$ placing Lyα within the KCWI wavelength range. In this work, we focus only on galaxies without obvious spectroscopic or photometric evidence for the presence of an AGN, and have therefore excluded 14 objects with spectroscopic evidence for the presence of AGN, to be discussed elsewhere. The remaining objects show no sign of significant AGN activity – e.g. they lack emission lines of high ionization species in the rest-UV KCWI and existing LRIS spectra, their nebular line ratios in the rest-frame optical are consistent with stellar excitation based on spectra taken with Keck/MOSFIRE (see e.g. Steidel et al. 2014), they lack power-law SEDs in the near-IR–mid-IR, etc. Because measurements of galaxy morphology are important to the analysis, we considered only the subset of the star-forming (non-AGN) galaxies that have also been observed at high spatial resolution using *HST* imaging or Keck/OSIRIS IFU spectroscopy behind adaptive optics (Section 3.2).

In addition to the known KBSS targets, many of the KCWI pointings include continuum-detected serendipitous galaxies whose KCWI spectra constitute the first identification of their redshifts. A total of 50 galaxies with $z > 2$ (most of which are fainter in the optical continuum than the KBSS limit of R = 25.5) have been identified. We have included 10 such objects in our analysis sample, based on their having *HST* observations with sufficient S/N for determination of morphology.

A minimum total integration of 2.5 h (5 h is more typical) at the position of a galaxy in the KCWI data cube was also imposed, in order to ensure the relative uniformity of the data set. Ultimately, after inspection of the high-resolution images (Section 3.2), six galaxies were removed because of source ambiguity or obvious contamination from nearby unrelated objects in the images, and two were excluded because they were not sufficiently resolved by *HST* to measure their position angle (PA) reliably (see Section 4).

The final sample to be considered in this work contains 59 galaxies, listed in Table 1. The redshifts given in Table 1 are based on MOSFIRE nebular spectra for 38 of the 59 galaxies, which have a precision of ∼±20 km s^{-1} and should accurately reflect the galaxy systemic redshift. In the remaining cases, features in the rest-frame UV spectra including Lyα emission and strong interstellar absorption features (e.g. Si II, Si IV, C II, C IV, O I) were used to estimate the systemic redshift of the galaxy, using the calibration described by Chen et al. (2020b). Briefly, the method uses the statistics –

Table 1. Summary of the galaxy sample and the observations.

Object[a] Identifier	RA (J2000.0)	DEC (J2000.0)	t_{exp} (KCWI) (hr)	Redshift[b]	$W_\lambda(Ly\alpha)$[c] (Å)	$F_{Ly\alpha}$(tot)[d] 10^{-17} erg s^{-1} cm^{-2}	$\frac{F_{Ly\alpha}(\text{blue})}{F_{Ly\alpha}(\text{red})}$[e]	Imaging[f] Data	PA$_0$[g] (deg)	PA$_0$[h] Method
Q0100-BX210	01:03:12.02	+13:16:18.5	5.4	2.2769	−3 ± 2	6.3 ± 0.5	0.08 ± 0.05	F160W	37	(i), (ii)
Q0100-BX212	01:03:12.51	+13:16:23.2	5.2	2.1063	−4 ± 3	2.3 ± 0.7	0.5 ± 0.29	F160W	−57	(i), (ii)
Q0100-C7	01:03:08.24	+13:16:30.1	5.1	3.0408	12 ± 1	9.0 ± 0.4	0.15 ± 0.03	F160W	16	(i), (ii)
Q0100-D11	01:03:08.25	+13:16:37.6	5.1	2.5865	6 ± 1	1.7 ± 0.4	0.11 ± 0.14	F160W	−12	(i), (ii)
Q0142-BX165	01:45:16.87	−09:46:03.5	5.0	2.3576	51 ± 3	37.5 ± 0.5	0.28 ± 0.01	F160W	14	(ii)
Q0142-BX188	01:45:17.79	−09:45:05.6	5.3	2.0602	−6 ± 1	4.6 ± 0.7	0.47 ± 0.15	F160W	66	(i), (ii)
Q0142-BX195-CS10	01:45:17.11	−09:45:06.0	4.5	2.7382 (UV)	−1 ± 3	2.2 ± 0.5	0.47 ± 0.24	F160W	29	(ii)
Q0142-NB5859	01:45:17.54	−09:45:01.2	5.8	2.7399 (UV)	20 ± 2	3.7 ± 0.4	0.65 ± 0.14	F160W	42	(i), (ii)
Q0207-BX144	02:09:49.21	−00:05:31.7	5.0	2.1682	25 ± 3	44.9 ± 0.6	0.29 ± 0.01	F140W	−74	(i), (ii)
Q0207-MD60	02:09:53.69	−00:04:39.8	4.3	2.5904	−27 ± 2	1.4 ± 0.5	− 0.16 ± 0.21	F140W	−64	(ii)
Q0449-BX88	04:52:14.94	-16:40:49.3	6.3	2.0086	−7 ± 3	3.3 ± 0.8	0.16 ± 0.16	F160W	10	(ii)
Q0449-BX88-CS8	04:52:14.79	-16:40:58.6	5.2	2.0957 (UV)	4 ± 1	3.9 ± 0.8	0.34 ± 0.17	F160W	−39	(i), (ii)
Q0449-BX89	04:52:14.80	-16:40:51.1	6.3	2.2570 (UV)	22 ± 2	7.6 ± 0.4	0.05 ± 0.03	F160W	−32	(i), (ii)
Q0449-BX93	04:52:15.41	-16:40:56.8	6.3	2.0070	−7 ± 2	7.4 ± 0.8	0.6 ± 0.13	F160W, OSIRIS	−18	(i), (ii), (iii)
Q0449-BX110	04:52:17.20	-16:39:40.6	5.0	2.3355	35 ± 2	20.4 ± 0.6	0.47 ± 0.03	F160W	−48	(i), (ii)
Q0821-MD36	08:21:11.41	+ 31:08:29.4	2.7	2.583	75 ± 10	23.1 ± 0.6	0.16 ± 0.02	F140W	37	(i), (ii)
Q0821-MD40	08:21:06.96	+ 31:07:22.8	4.3	3.3248	27 ± 3	11.0 ± 0.4	0.34 ± 0.03	F140W	−7	(ii)
Q1009-BX215	10:11:58.71	+ 29:41:55.9	4.0	2.5059	1 ± 1	3.7 ± 0.8	0.34 ± 0.15	F160W	−20	(i), (ii)
Q1009-BX218	10:11:58.96	+ 29:42:07.5	5.3	2.1091	−6 ± 3	4.0 ± 0.6	0.18 ± 0.11	F160W	−43	(i), (ii)
Q1009-BX222	10:11:59.09	+ 29:42:00.5	5.3	2.2031	−4 ± 1	4.7 ± 0.5	0.28 ± 0.08	F160W	−83	(i), (ii)
Q1009-BX222-CS9	10:11:58.92	+ 29:42:02.6	5.3	2.6527 (UV)	−1 ± 4	1.0 ± 0.4	−	F160W	76	(i), (ii)
Q1009-D15	10:11:58.73	+ 29:42:10.5	5.3	3.1028 (UV)	−18 ± 6	4.2 ± 0.4	0.28 ± 0.08	F160W	28	(i), (ii)
Q1549-BX102	15:51:55.98	+ 19:12:44.2	5.0	2.1934	50 ± 3	19.5 ± 0.5	0.51 ± 0.03	F606W	−87	(i), (ii)
Q1549-M17	15:51:56.06	+ 19:12:52.7	3.3	3.2212 (UV)	27 ± 5	4.3 ± 0.5	0.0 ± 0.05	F606W	72	(ii)
Q1623-BX432	16:25:48.74	+ 26:46:47.1	3.6	2.1825	17 ± 1	10.8 ± 0.7	0.46 ± 0.06	F160W	16	(ii)
Q1623-BX436	16:25:49.10	+ 26:46:53.4	3.6	2.0515 (UV)	−12 ± 2	2.6 ± 1.0	−	F160W	12	(ii)
Q1623-BX453	16:25:50.85	+ 26:49:31.2	4.8	2.1821	10 ± 2	2.8 ± 0.5	0.33 ± 0.14	F160W, OSIRIS	31	(iii)
Q1623-BX453-CS3	16:25:50.35	+ 26:49:37.1	4.7	2.0244 (UV)	17 ± 2	5.6 ± 0.9	0.3 ± 0.11	F160W	−66	(i), (ii)
Q1623-C52	16:25:51.20	+ 26:49:26.3	4.8	2.9700 (UV)	4 ± 1	8.5 ± 0.4	0.22 ± 0.03	F160W	−13	(ii)
Q1700-BX490	17:01:14.83	+ 64:09:51.7	4.3	2.3958	−3 ± 4	12.8 ± 0.5	0.39 ± 0.03	F814W, OSIRIS	86	(i), (ii), (iii)
Q1700-BX561	17:01:04.18	+ 64:10:43.8	5.0	2.4328	−3 ± 3	8.5 ± 0.6	0.51 ± 0.08	F814W	9	(ii)
Q1700-BX575	17:01:03.34	+ 64:10:50.9	5.0	2.4334	0 ± 2	5.2 ± 0.6	0.14 ± 0.08	F814W	−34	(i), (ii)
Q1700-BX581	17:01:02.73	+ 64:10:51.3	4.7	2.4022	9 ± 4	10.6 ± 0.7	0.28 ± 0.05	F814W	27	(i), (ii)
Q1700-BX710	17:01:22.13	+ 64:12:19.3	5.0	2.2946	−10 ± 3	8.1 ± 0.6	0.51 ± 0.09	F814W	−19	(i), (ii)
Q1700-BX729	17:01:27.77	+ 64:12:29.5	4.7	2.3993	14 ± 2	12.9 ± 0.5	0.17 ± 0.03	F814W	−3	(i), (ii)
Q1700-BX729-CS4	17:01:28.95	+ 64:12:32.4	3.0	2.2921 (UV)	14 ± 3	5.8 ± 1.1	0.21 ± 0.12	F814W	40	(ii)
Q1700-BX729-CS9	17:01:27.49	+ 64:12:25.1	4.7	2.4014 (UV)	35 ± 2	1.1 ± 0.5	− 0.19 ± 0.21	F814W	−59	(i), (ii)
Q1700-MD103	17:01:00.21	+ 64:11:55.6	5.0	2.3151	−24 ± 1	− 0.5 ± 0.5	−	F814W	55	(ii)
Q1700-MD104	17:01:00.67	+ 64:11:58.3	5.0	2.7465 (UV)	6 ± 2	8.2 ± 0.4	0.11 ± 0.03	F814W	7	(i), (ii)
Q1700-MD115	17:01:26.68	+ 64:12:31.7	4.7	2.9081 (UV)	33 ± 7	7.8 ± 0.5	0.05 ± 0.03	F814W	3	(i), (ii)
Q2206-MD10	22:08:52.21	-19:44:13.9	5.0	3.3269	5 ± 2	4.0 ± 0.5	0.07 ± 0.08	F160W	41	(i), (ii)
DSF2237b-MD38	22:39:35:64	+ 11:50:27.5	3.7	3.3258	2 ± 2	3.0 ± 0.5	0.44 ± 0.16	F606W	52	(i), (ii)

Table 1 – *continued*

Object[a] Identifier	RA (J2000.0)	DEC (J2000.0)	t_{exp} (KCWI) (hr)	Redshift[b]	$W_\lambda(Ly\alpha)$[c] (Å)	$F_{Ly\alpha}$(tot)[d] 10^{-17} erg s^{-1} cm^{-2}	$\frac{F_{Ly\alpha}(\text{blue})}{F_{Ly\alpha}(\text{red})}$ [e]	Imaging[f] Data	PA$_0$ [g] (deg)	PA$_0$ [h] Method
Q2343-BX379	23:46:28.96	+12:47:26.0	4.0	2.0427 (UV)	−7 ± 2	6.4 ± 1.3	0.64 ± 0.23	F140W	−60	(i), (ii)
Q2343-BX389	23:46:28.90	+12:47:33.5	4.0	2.1712	−16 ± 1	1.6 ± 0.6	0.65 ± 0.49	F140W	−50	(ii)
Q2343-BX391	23:46:28.07	+12:47:31.8	4.0	2.1738	−16 ± 1	3.3 ± 0.7	–	F140W	21	(i), (ii)
Q2343-BX417	23:46:26.27	+12:47:46.7	3.0	2.2231 (UV)	−9 ± 6	4.8 ± 0.7	0.49 ± 0.15	F160W	−38	(ii)
Q2343-BX418	23:46:18.57	+12:47:47.4	4.9	2.3054	46 ± 3	40.5 ± 0.6	0.46 ± 0.01	F140W, OSIRIS	2	(i), (ii), (iii)
Q2343-BX418-CS8	23:46:18.73	+12:47:51.6	5.1	2.7234 (UV)	66 ± 15	6.7 ± 0.4	0.15 ± 0.04	F140W	−67	(i), (ii)
Q2343-BX429	23:46:25.26	+12:47:51.2	5.2	2.1751	−8 ± 5	3.0 ± 0.5	0.31 ± 0.15	F160W	28	(i), (ii)
Q2343-BX442	23:46:19.36	+12:47:59.7	4.6	2.1754	−18 ± 4	1.6 ± 0.7	0.38 ± 0.52	OSIRIS	−12	(iv)
Q2343-BX513	23:46:11.13	+12:48:32.1	4.8	2.1082	10 ± 1	18.6 ± 0.7	0.71 ± 0.05	F140W, OSIRIS	−9	(i), (ii), (iii)
Q2343-BX513-CS7	23:46:10.55	+12:48:30.9	4.8	2.0144 (UV)	−22 ± 2	4.2 ± 1.0	0.53 ± 0.26	F160W	71	(i), (ii)
Q2343-BX587	23:46:29.17	+12:49:03.4	5.2	2.2427	−4 ± 3	7.2 ± 0.5	0.22 ± 0.05	F160W	44	(i), (ii)
Q2343-BX587-CS3	23:46:28.24	+12:49:07.2	4.8	2.5727 (UV)	2 ± 2	1.3 ± 0.4	0.17 ± 0.26	F140W	−53	(i), (ii)
Q2343-BX587-CS4	23:46:28.62	+12:49:04.8	5.2	2.8902 (UV)	−13 ± 1	2.8 ± 0.4	0.08 ± 0.08	F140W	−59	(i), (ii)
Q2343-BX610	23:46:09.43	+12:49:19.2	5.3	2.2096	8 ± 2	13.5 ± 0.7	0.26 ± 0.04	F140W	22	(ii)
Q2343-BX660	23:46:29.43	+12:49:45.6	5.0	2.1742	20 ± 3	25.7 ± 0.6	0.26 ± 0.02	F140W, OSIRIS	37	(i), (ii), (iii)
Q2343-BX660-CS7	23:46:29.82	+12:49:38.7	4.2	2.0788 (UV)	41 ± 1	2.3 ± 0.9	–	F140W	89	(ii)
Q2343-MD80	23:46:10.80	+12:48:33.2	4.8	2.0127	−26 ± 3	2.8 ± 0.8	0.22 ± 0.24	F140W	9	(i), (ii)

[a]The 'CS' objects are continuum serendipitous objects discussed in Section 2. Their naming follows nearby KBSS galaxies that are previously known and may not be physically associated to the CS objects.
[b]If marked as 'UV', the systemic redshift was estimated from features in the rest-UV spectra, calibrated as described by Chen et al. (2020b). The typical uncertainties on UV-estimated systemic redshifts are $\delta v \equiv c\delta z_{sys}/(1 + z_{sys}) \simeq 100$ km s^{-1}. Otherwise, z_{sys} was measured from nebular emission lines in rest-optical (MOSFIRE) spectra, with $\delta v \simeq 20$ km s^{-1}.
[c]Rest-frame Lyα equivalent width. Details discussed in Section 2.
[d]Total Lyα flux. See Section 6 for more details.
[e]Flux ratio between the blueshifted and redshifted components of Lyα emission. Details in Section 6.
[f]F140W and F160W images obtained using *HST*-WFC3-IR, F606W, and F814W images from *HST*−ACS.
[g]Typical uncertainty: ±10°.
[h]Methods used to measure PA$_0$: (i) using GALFIT on *HST* images; (ii) using the pixel intensity second moment on *HST* images; (iii) pixel intensity second moment on OSIRIS Hα map; and (iv) kinematics of Hα emission. Details on the methods are shown in Section 4.2.
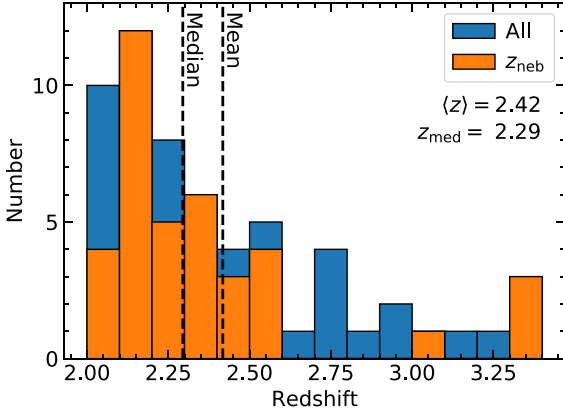
Figure 1. Redshift distribution of the galaxy sample. The blue histogram represents the full sample of 59 galaxies. The orange histogram shows the distribution for the 38 galaxies with nebular redshift measurements from MOSFIRE near-IR spectra, while the rest are calibrated based on Chen et al. (2020b) using rest-UV absorption lines or Lyα emission from Keck/LRIS and/or KCWI spectra. The mean (median) redshift of the full sample is 2.42 (2.29).

based on several hundred KBSS galaxies with both nebular and UV observations – of the velocity offsets between nebular redshifts and redshifts defined by UV spectral features for samples divided by their UV spectral morphology, i.e. Lyα emission only, Lyα emission and interstellar absorption, or interstellar absorption only. The mean offsets for the appropriate sub-sample were applied to the UV-based redshifts in cases where nebular redshifts are not available; systemic redshifts obtained using such calibrations have an uncertainty of $\simeq$ 100 km s^{-1} when the rest-UV spectra are of high quality (see e.g. Steidel et al. 2018). Fig. 1 shows the redshift distribution of the KCWI sample, which has $z_{med} = 2.29 \pm 0.40$ (median and standard deviation), for which the conversion between angular and physical scales is 8.21 pkpc/″ with our assumed cosmology.

Reliable SED fits are available for 56 of the 59 galaxies using the BPASSv2.2 stellar population synthesis model (Stanway & Eldridge 2018) and SMC extinction curve. This choice of SED model has been shown to predict internally consistent stellar mass (M_*) and SFR for high-redshift galaxies having properties similar to those in our sample (see e.g. Steidel et al. 2016; Strom et al. 2017; Theios et al. 2019), i.e. $8.5 \lesssim \log(M_*/M_\odot) \lesssim 11$ and $1 \lesssim \mathrm{SFR}/(M_\odot \, \mathrm{yr}^{-1}) \lesssim$ 100. The distributions of M_* and SFR (Fig. 2) are similar to those of the full KBSS galaxy sample, albeit with a slight over-representation of $\log(M_*/M_\odot) \lesssim 9$ galaxies[1].

In order to facilitate comparison of the Lyα emission line strength of sample galaxies with those in the literature, Table 1 includes the rest-frame Lyα equivalent width ($W_\lambda(\mathrm{Ly}\alpha)$) based on extraction of 1D spectra from the KCWI data cubes over a spatial aperture defined by the extent of the UV continuum light of each galaxy.[2]

---

[1]For direct comparison of our sample with the so-called 'star formation main sequence' (SFMS), we note that SED fits that assume solar metallicity SPS models from Bruzual & Charlot (2003) and attenuation curve from Calzetti et al. (2000) result in a distribution of SFR versus M_* entirely consistent with the published SFMS at $z \sim 2$ (e.g. Whitaker et al. 2014).

[2]In general, the Lyα emission evaluated within a central aperture represents only a fraction of the total that would be measured in a large aperture that accounts for the diffuse Lyα haloes with spatial extent well beyond that of the FUV continuum (see e.g. Steidel et al. 2011; Wisotzki et al. 2016); however,
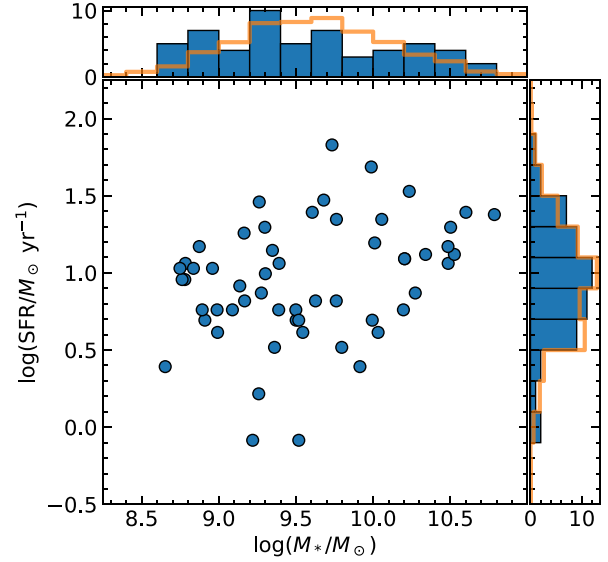
Figure 2. Distribution of SFR and M_* of 56/59 galaxies in this sample; the remaining three galaxies have insufficient photometric measurements for reliable SED fitting. The normalized distributions of the parent KBSS sample are shown in the orange 1D histograms. The SFR and M_* of galaxies used in this work are similar to those of the parent KBSS sample; the values are all based on the BPASS-v2.2-binary spectral synthesis models (Stanway & Eldridge 2018), assuming stellar metallicity $Z = 0.002$, SMC extinction as described by Theios et al. (2019), and a Chabrier (2003) stellar initial mass function.

The values of $W_\lambda(\mathrm{Ly}\alpha)$ in Table 1 were measured using the method described in Kornei et al. (2010) (see also Reddy & Steidel 2009), where positive values indicate net emission and negative values indicate net absorption. Aside from a slight over-representation of galaxies with the strongest Lyα emission ($W_\lambda(\mathrm{Ly}\alpha) \gtrsim$ 40 Å), the sample in Table 1 is otherwise typical of UV-continuum-selected galaxies in KBSS by construction. The $W_\lambda(\mathrm{Ly}\alpha)$ distribution for the sample in Table 1 is shown in Fig. 3. In addition to $W_\lambda(\mathrm{Ly}\alpha)$, we also measured the total Lyα flux ($F_{\mathrm{Ly}\alpha}$) and the ratio between the blue- and redshifted components of emission for the entire Lyα halo ($F_{\mathrm{Ly}\alpha}(\mathrm{blue})/F_{\mathrm{Ly}\alpha}(\mathrm{red})$), which are discussed further in Section 6.

3 OBSERVATIONS AND REDUCTIONS

3.1 KCWI

The KCWI data discussed in the present work were obtained between 2017 September and 2020 November, in all cases using the medium-scale slicer made up of 24 slices of width 0″.69 and length 20″.3 on the sky. The instrumental setup uses the BL volume phase holographic grating with an angle of incidence that optimizes the diffraction efficiency near 4200 Å, with the camera articulation angle set to record the spectra of each slice with a central wavelength of ∼4500 Å. A band-limiting filter was used to suppress wavelengths outside of the range of 3500–5600 Å to reduce scattered light; the useful common wavelength range recorded for all 24 slices in this mode is 3530–5530 Å, with a spectral resolving power ranging from $R \simeq$ 1400 at 3530 Å to $R \simeq$ 2200 at 5530 Å. At the mean redshift of the

the central $W_\lambda(\mathrm{Ly}\alpha)$ is a closer approximation to values measured in most spectroscopic galaxy surveys.
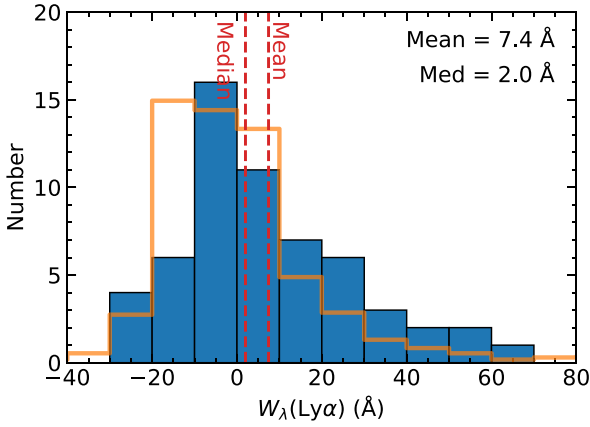
Figure 3. Distribution of $W_\lambda(\mathrm{Ly}\alpha)$ for the sample (blue histogram). The orange skeletal histogram shows the normalized $W_\lambda(\mathrm{Ly}\alpha)$ distribution from Reddy & Steidel ([2009](#)), which is a subset of the current KBSS sample large enough to be representative. The sample discussed in this work is slightly biased towards Ly α-emitting galaxies compared to the parent sample of $z \sim$ 2–3 KBSS galaxies.

sample ($\langle z \rangle = 2.42$), Ly α falls at an observed wavelength of ~4160 Å, where $R \sim 1650$.

The E2V 4k × 4k detector was binned 2 × 2, which provides spatial sampling along slices of $0\rlap{.}''29$ pix^{-1}. Because each slice samples $0\rlap{.}''68$ in the dispersion direction, the effective spatial-resolution element is rectangular on the sky, with an aspect ratio of ~2.3 : 1. We adopted the following approach to the observations, designed to ensure that the slicer geometry with respect to the sky is unique on each 1200-s exposure so that the effective spatial resolution on the final stacked data cube is close to isotropic. Typically, a total integration of ~5 h is obtained as a sequence of 15 exposures of 1200 s, each obtained with the sky PA of the instrument rotated by 10–90 degrees with respect to adjacent exposures. Each rotation of the instrument FoV is accompanied by a small offset of the telescope pointing before the guide star is reacquired. In this way, a given sky position is sampled in 15 different ways by the slicer.

3.1.1 KCWI data reduction

Each 1200-s exposure with KCWI was initially reduced using the data reduction pipeline (DRP) maintained by the instrument team and available via the Keck Observatory web site.[3] The DRP assembles the 2D spectra of all slices into a 3D data cube (with spaxels of $0\rlap{.}''29 \times 0\rlap{.}''69$, the native scale) using a suite of procedures that can be customized to suit particular applications. The procedures include cosmic ray removal, overscan subtraction and scattered light subtraction, wavelength calibration, flat-fielding, sky subtraction, differential atmospheric refraction (DAR) correction, and flux calibration. Wavelength calibration was achieved using ThAr arc spectra obtained using the internal calibration system during the afternoon prior to each observing night. Flat-fielding was accomplished using spectra of the twilight sky at the beginning or end of each night, after dividing by a b-spline model of the solar spectrum calculated using the information from all slices. For each frame, the sky background was subtracted using the sky-modelling feature in the DRP, after which the sky-subtracted image (still in the 2D format) is examined

in order to mask pixels, in all 24 slices, that contain significant light from sources in the field. The frame was then used to make a new 2D sky model using only unmasked pixels, and the sky-subtracted image is reassembled into a wavelength-calibrated (rebinned to 1 Å per wavelength bin) data cube, at which time a variance cube, an exposure cube, and a mask cube are also produced.

Next, we removed any remaining low-frequency residuals from imperfect sky background subtraction by forming a median-filtered cube after masking obvious continuum and extended emission line sources using a running 3D boxcar filter. The typical dimensions of the filter are 100 Å (100 pixels) in the wavelength direction, 16 pixels ($4\rlap{.}''6$) along slices, and 1 pixel ($0\rlap{.}''69$) perpendicular to the slices, with the last ensuring slice-to-slice independence. Minor adjustments to the filter dimensions were made as needed. If the running boxcar encounters a large region with too few unmasked pixels to allow a reliable median determination, then the pixel values in the filtered cube were interpolated from the nearest adjacent regions for which the median was well determined. Finally, the median-filtered cube for each observed frame was subtracted from the data. We found that this method proved effective for removing scattered light along slices caused by bright objects within the KCWI FoV.

Because neither Keck II nor KCWI has an atmospheric dispersion corrector, each cube is corrected for DAR (i.e. apparent position of an object as a function of wavelength) using the elevation and parallactic angle at the midpoint of the exposure and a model of the atmosphere above Maunakea. Finally, each cube was flux-calibrated using observations obtained with the same instrument configuration of one or more spectrophotometric standard stars selected from a list recommended by the KCWI documentation.

Prior to stacking reduced data cubes of individual exposures covering the same sky region, they must be aligned spatially and rotated to account for differences in the PA of the instrument with respect to the sky on different exposures. To accomplish this, we averaged the DAR-corrected cubes along the wavelength axis to create pseudo-white-light images, rotated each to the nominal sky orientation (N up and E left) based on the World Coordinate System (WCS) recorded in the header, and cross-correlated the results to determine the relative offsets in RA and Dec, which we found to have a precision of $\simeq 0.03$ arcsec (root-mean-square, RMS). The offsets were applied to the WCS in the header of each cube, and all cubes for a given pointing were then resampled to a common spatial grid with spatial sampling of $0\rlap{.}''3 \times 0\rlap{.}''3$ using a 2D *drizzle* algorithm in the *Montage* package,[4] with drizzle factor of 0.7. If the wavelength grid is different among cubes, the spectrum in each spaxel was resampled to a common grid using cubic spline. Finally, we stacked the resampled cubes by averaging, weighted by exposure time. A white light image of the final stacked data cube was used to determine small corrections to the fiducial RA and Dec to align with other multiwavelength data of the same region.

3.2 High spatial-resolution imaging

For galaxies in the mass range of our sample at $z \sim 2.5$, the typical half-light diameter is ~4 pkpc, which corresponds to $\simeq 0\rlap{.}''5$ (Law et al. [2012b](#)). To obtain reliable measurements of the orientation of the galaxy's projected major and minor axes (see Section 4), high-resolution images are crucial. We gathered existing data from two sources: space-based optical or near-IR images from the *HST*/ACS or the *HST*/WFC3; alternatively, H α maps obtained using

Table 2. Summary of *HST* observations.

Field	Inst.	Filter	Prog. ID	PI	t_{exp} (s)[a]
DSF2237b	ACS	F606W	15287	A. Shapley[b]	6300
Q0100	WFC3	F160W	11694	D. Law[c]	8100
Q0142	WFC3	F160W	11694	D. Law[c]	8100
Q0207	WFC3	F140W	12471	D. Erb	800
Q0449	WFC3	F160W	11694	D. Law[c]	8100
Q0821	WFC3	F140W	12471	D. Erb	800
Q1009	WFC3	F160W	11694	D. Law[c]	8100
Q1549	ACS	F606W	12959	A. Shapley[d]	12000
Q1623	WFC3	F160W	11694	D. Law[c]	8100
Q1700	ACS	F814W	10581	A. Shapley[e]	12500
Q2206	WFC3	F160W	11694	D. Law[c]	8100
Q2343	WFC3	F140W	14620	R. Trainor	5200
Q2343	WFC3	F160W	11694	D. Law[c]	8100

[a]Defined as the median exposure time across the whole FoV.
[b]Pahl et al. (2021).
[c]Law et al. (2012c) and Law et al. (2012b).
[d]Mostardi et al. (2015).
[e]Peter et al. (2007).

the Keck/OSIRIS integral field spectrometer (Larkin et al. 2006) behind the WMKO laser guide star adaptive optics system, which typically provides spatial resolution of 0″.11–0″.15 (Law et al. 2007, 2009, 2012a).

The *HST*/WFC3-IR images in this work were obtained using either the F140W or F160W filters, from programs listed in Table 2, with spatial resolution of ∼0″.16 and∼0″.18, respectively. The *HST*/ACS images were taken in either the F606W or F814W filters, with spatial resolution of ∼0″.09 (full width at half-maximum; FWHM). In all cases, overlapping exposures were aligned and combined using *DrizzlePac*.[5] For the Q2343 field, where galaxies have been observed with comparably deep observations in two filters, we selected the image with the smaller estimated uncertainty in the measured PA (see Section 4.2). The Keck/OSIRIS Hα maps of six galaxies included in the sample are presented by Law et al. (2007), Law et al. (2009), Law et al. (2012a), and Law et al. (2018); details of the observations and data reduction can be found in those references.

4 GALAXY AZIMUTHAL ANGLE

4.1 Motivation

The physical state of the CGM is controlled by the competition between accretion of new material on to the galaxy and outflows driven by processes originating at small galactocentric radii. In what one might call the 'classic' picture (see Veilleux, Cecil & Bland-Hawthorn 2005; Tumlinson et al. 2017 for review articles), based on observations of nearby starburst galaxies, inflowing and outflowing gas occurs preferentially along the major and minor axes, respectively, as in the schematic diagram in Fig. 4. It is well established around star-forming galaxies at $z \lesssim 1$ that outflows driven by energy or momentum from stellar feedback (radiation pressure from massive stars, supernovae) originating near the galaxy centre tend to escape along the direction that minimizes the thickness of the ambient interstellar medium (ISM) that would tend to slow or prevent outflows from escaping the galactic disc. Meanwhile, accretion of cool gas from the intergalactic medium (IGM) is believed to occur in quasi-collimated filamentary flows that carry significant angular

[5]https://www.stsci.edu/scientific-community/software/drizzlepac
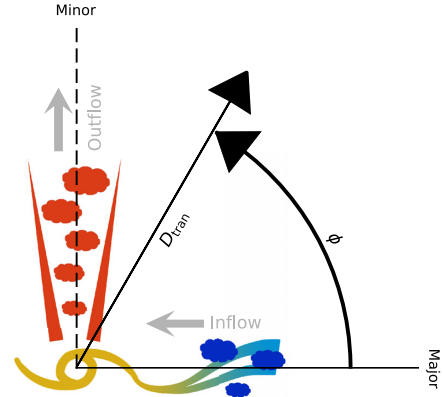
Figure 4. A schematic diagram of how the galaxy azimuthal angle (ϕ) is defined in this work and how it might be related to the origin and kinematics of gas in the CGM under common assumptions of a bi-conical outflow with accretion along the disc plane. Suppose that we are viewing a galaxy projected on the sky in this diagram, naively, one would expect to see inflow aligning with the projected galaxy major axis and outflow aligning with the minor axis. Impact parameter, D_{tran}, is defined as the projected distance from the centre of the galaxy. The galaxy azimuthal angle, ϕ, is defined as the projected angle on the sky with respect to the centre of the galaxy and starts from the projected galaxy major axis.

momentum and thus would tend to approach the inner galaxy in a direction parallel to the disc plane (Nelson et al. 2019; Péroux et al. 2020). If feedback processes are sufficiently vigorous, the accretion is also most likely along directions that do not encounter strong outflows. When projected on to the plane of the sky, these considerations would tend to intersect outflowing material along the polar direction (the projected minor axis) and accreting material when the azimuthal angle (see Fig. 4) is closer to the PA of the projected major axis.

At redshifts $z \lesssim 1$, there is strong support for this general geometric picture from the statistics of the incidence and strength of rest-UV absorption lines observed in the spectra of background sources, as a function of the azimuthal angle of the vector connecting the sightline and the centre of the galaxy. As might be expected from a picture similar to Fig. 4, sightlines with ϕ close to the minor axis intersect gas with a large range of velocities, which kinematically broadens the observed absorption complexes comprising many saturated components (e.g. Bordoloi et al. 2011; Bouché et al. 2012; Kacprzak et al. 2012; Schroetter et al. 2019). For azimuthal angles ϕ close to the major axis, the absorption features are strong due to the high covering fraction and column density of low ionization gas near the disc plane and broadened by the kinematics of differential rotation. The same picture has been supported by cosmological simulations where the gas metallicity, radial velocity, and the amount of outflowing mass all show significant differences along the galaxy major and minor axes (Nelson et al. 2019; Péroux et al. 2020).

It remains unclear, however, whether this geometric picture should be applied to galaxies at $z \sim 2$, where a large fraction of galaxies, particularly those with $\log(M_*/M_\odot) \lesssim 10$, appear to be 'dispersion dominated', where the rotational component of dynamical support (V_{rot}) is significantly smaller than that of apparently random motion (σ) (Förster Schreiber et al. 2009; Law et al. 2009), and where the central dynamical mass of the galaxy may be dominated by cold gas rather than stars – and therefore any disc would be highly unstable. For such galaxies, there is not always a clear connection between the morphology of starlight and the principal kinematic

axes (e.g. Erb et al. 2004; Law et al. 2012b). Meanwhile, a WFC3 survey conducted by Law et al. (2012b) for similar galaxies strongly supports 3D triaxial morphology, instead of inclined disc, to be the most suitable model to describe these galaxies. The fact that the vast majority of galaxies with DTB spectra at $z > 2$ have systematically blueshifted interstellar absorption lines and systematically redshifted Lyα emission suggests that outflows cannot be confined to a small range of azimuth (Shapley et al. 2003; Steidel et al. 2010; Jones, Stark & Ellis 2012 etc.).

The spatial and spectral distribution of the Lyα emission surrounding galaxies may provide crucial insight into the degree of axisymmetry and the dominant magnitude and direction of gas flows in the CGM. In any case, IFU observations of Lyα, where both the geometry and the kinematics of the extended emission can be mapped, complement information available from absorption line studies.

In the analysis below, we define the galaxy azimuthal angle (ϕ) as the absolute angular difference between the vector connecting the galaxy centroid and a sky position at projected angular distance of θ_{tran} (or projected physical distance D_{tran}) and PA_0, the PA of the galaxy major axis measured from the galaxy stellar continuum light, as illustrated schematically in Fig. 4,

$$\phi = |PA - PA_0|. \tag{1}$$

The zero-point for measurements of PA is arbitrary, but for definiteness we measure PA as degrees east (E) of north (N), so that angles increase in the counter-clockwise direction when N is up and E to the left. The use of equation (1) to define ϕ implies that $0 \leq \phi/\text{deg} \leq 90$, and that $\phi = 0$ (90) deg corresponds to the projected major (minor) axis.

4.2 Methods

In order to obtain reliable measurements of ϕ, it is important to measure PA_0 accurately and consistently. We used up to four different methods to determine PA_0 for each galaxy. The choice of method depends on the information available; these are briefly summarized as follows:

(i) *Sérsic profile fitting of HST images*: In this method, we fit a 2D Sérsic profile (Sérsic 1963) to the host galaxy by using GALFIT (Peng et al. 2002, 2010) and determined PA_0 from the best-fitting model parameters. The point spread function (PSF) was measured by selecting stellar sources over the full *HST* pointing using the star classifier in *SExtractor*, which calculates a 'stellarity index' for each object based on a neural network. We then examined sources with the highest 3 per cent stellarity indices by eye and normalized and stacked them to form an empirical PSF. Our fiducial model consists of a 2D elliptical Sérsic profile convolved with the PSF. We also included the first-order Fourier mode to handle the asymmetric morphology in most cases. However, over- or under-fitting can cause failure of convergence or unreasonably large fitting errors and residuals. In most cases, the cause of the failure and the required adjustment are obvious in the original galaxy image and the model residual. For example, if the residual reveals an additional source, we would add an additional Sérsic component or a simple scaled PSF to the model, depending on the size of the additional source. Meanwhile, if the primary source shows a triangular morphology, we would add the third-order Fourier mode[6] associated with the Sérsic profile. However, in certain cases, obtaining a successful

fit requires experimenting with the model by adding or removing certain degrees of freedom. The rule of thumb is that we add or remove degrees of freedom one at a time and adopt the adjustment if it makes the fit converge or significantly diminishes the reduced χ^2 and the fitted error of PA_0. In the end, 23 galaxies were fit with the fiducial model. Nine galaxies (Q0100-C7, Q0821-MD36, Q1009-BX222, Q1009-D15, Q1623-BX453-CS3, Q1700-BX729-CS9, Q2343-BX418, Q2343-BX418-CS8, and Q2343-BX660) were fit without the Fourier modes. Five galaxies (Q1009-BX218, Q1700-BX490, Q1700-BX710, Q1700-BX729, and Q2343-BX513-CS7) were fit with additional sources. Three galaxies (Q2343-BX391, Q2343-BX587-CS3, and Q2343-BX587-CS4) were fit with third-order Fourier modes. Galaxies with unsuccessful fits require using alternative methods, detailed below. Successful Sérsic fits were obtained for 40 of 59 galaxies, shown in Figs 5 and 7; galaxies with successful applications of this method tend to be isolated and to have a dominant central high SB component.

(ii) *Second moment of pixel intensity on HST images*: This method calculates the flux-weighted pixel PA arithmetically derived from the second moment of the pixel intensity,

$$\tan(2PA_0) = \frac{2\langle xy \rangle}{\langle x^2 \rangle - \langle y^2 \rangle}, \tag{2}$$

where x and y are the pixel positions relative to the centre of the galaxy in the x and y directions, and '$\langle ... \rangle$' indicates the arithmetic mean of the pixel coordinates weighted by pixel flux. Galaxy centres were defined as the point where $\langle x \rangle = 0$ and $\langle y \rangle = 0$. Especially for the galaxies that are morphologically complex, we found that the PA_0 measurements using this method are sensitive to the SB threshold used to define the outer isophotes and to the spatial resolution of the *HST* image. Therefore, all ACS images (which have higher spatial resolution than those taken with WFC3-IR) were convolved with a 2D Gaussian kernel to match the PSF to those of the WFC3-IR/F160W images. Among 59 galaxies, PA_0 of 58 galaxies can be otained using this method. They are shown in Figs 5, 6, and 7. We tested various SB thresholds and found that a threshold of 50 per cent of the peak SB after convolution provides the most consistent measurements between the PA_0 measured using (i) and (ii) has an rms of 10.8 degrees.

(iii) *Second moment of pixel intensity of OSIRIS Hα maps*: This method uses the same algorithm as in (ii), applied to Keck/OSIRIS Hα maps rather than *HST* continuum images. The SB threshold follows Law et al. (2009). There are six galaxies whose major axes were determined using this method, including one (Q1623-BX453) whose F160W image is unresolved. For the remaining five galaxies, the rms between PA_0 measured from the *HST* images and this method is ∼15 degrees. All six galaxies are shown in Fig. 7.

(iv) *Hα Kinematics*: As the only galaxy in this sample that demonstrates not only rotational kinematics from Hα emission but also clear disc morphology (Law et al. 2012a), the galaxy major axis of Q2343-BX442 is defined to be perpendicular to its rotational axis (Fig. 8). Because of its complex morphology, we did not apply method (i) to this galaxy. Method (ii) is likely dominated by the inner spiral structure and leads to a PA_0 that is ∼90 degrees apart from that determined from kinematics, while method (iii) is consistent with this method within 15 degrees.

Table 1 lists the adopted measurement of PA_0 for each galaxy in the sample, as well as the methods used to determine it. In cases where multiple methods were applied, we used the average PA_0 of the OSIRIS and *HST* measurements, where the latter value is an average of the results obtained using methods (i) and (ii). This way, more weight is given to method (iii) results when available, since it utilizes

---

[6]The second-order Fourier mode is degenerate with the ellipticity.
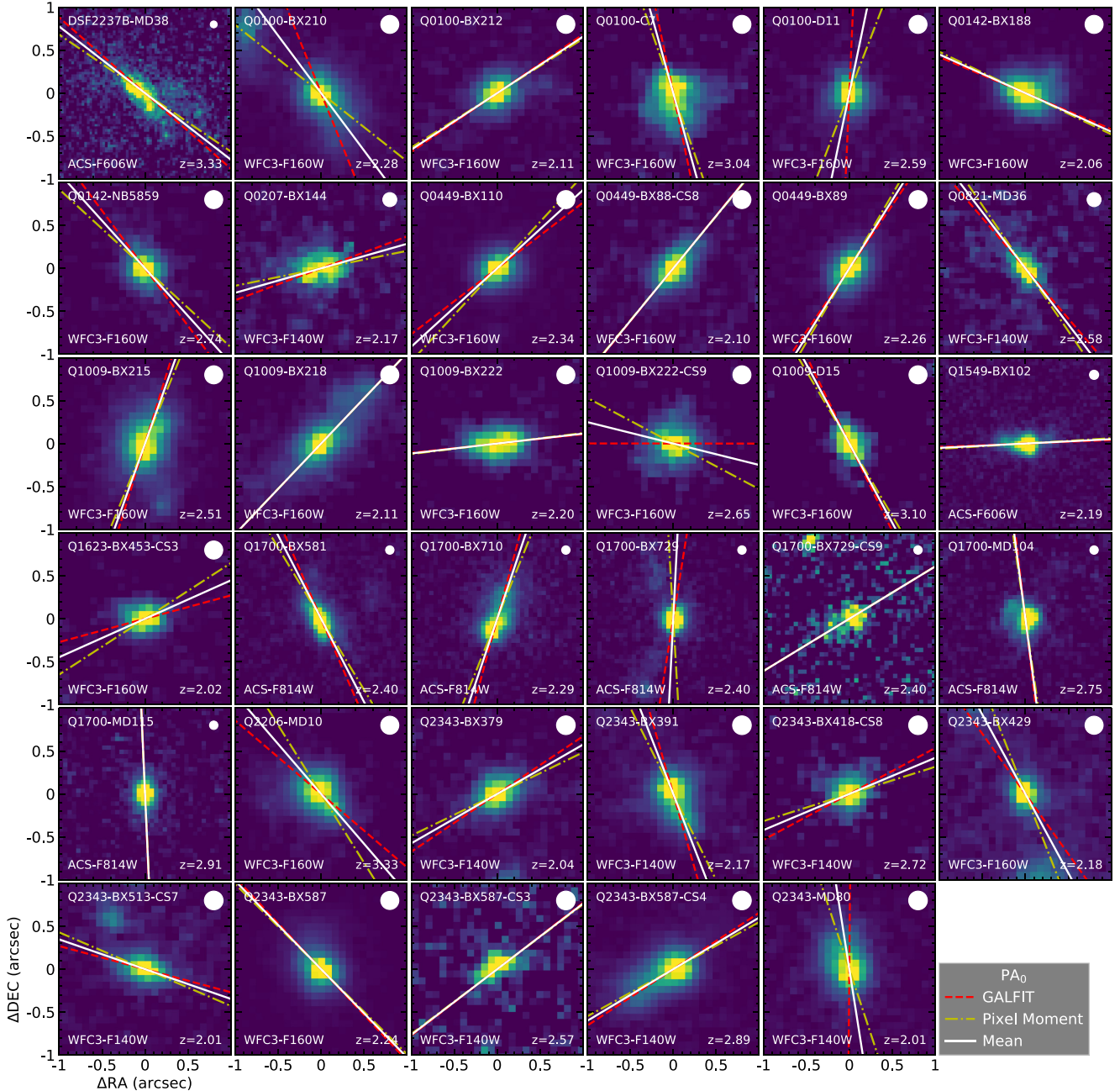
Figure 5. *HST* images of the 35 galaxies whose PA_0 were determined from methods (i) and (ii). For each image, shown in the four corners, from top left in clockwise direction, are the KBSS identifier, the FWHM of PSF, redshift, and the instrument and filter that the image was taken with. The dashed red line, dash-dotted yellow line, and the solid white line indicate the direction of PA_0 measured from GALFIT, pixel moment, and the average between the two.

entirely independent data from a different instrument. The robustness of PA_0 measurements is discussed in the following two subsections.

4.3 Relationship between the kinematic and morphological major axes

An important issue for the interpretation of morphological measurement of PA_0 is the extent to which it is likely to be a proxy for the *kinematic* major axis. Two of the 17 galaxies in Fig. 6 (Q2343-BX389 and Q2343-BX610) were studied as part of the SINS IFU survey by Förster Schreiber et al. (2018, hereafter FS18) and were subsequently re-observed with the benefit of adaptive optics by FS18; the latter

found that both have clear rotational signatures and that the inferred differences between their morphological major axis PA_0 and the kinematic major axis PA_{kin} are $\Delta PA \equiv |PA_0 - PA_{kin}| = 2 \pm 5$ deg and 27 ± 10 deg for Q2343-BX389 and Q2343-BX610, respectively. From their full sample of 38 galaxies observed at AO resolution, FS18 found $\langle \Delta PA \rangle = 23$ degrees (mean), with median $\Delta PA_{med} = 13$ degrees.

Among the six galaxies that also have $H\alpha$ velocity maps from Law et al. (2009) (used for method (iii) above), two (Q0449-BX93 and Q1623-BX453) show no clear rotational signature, so that PA_{kin} is indeterminate. Small amounts of velocity shear were observed for Q2343-BX513 and Q2343-BX660, both having PA_{kin}
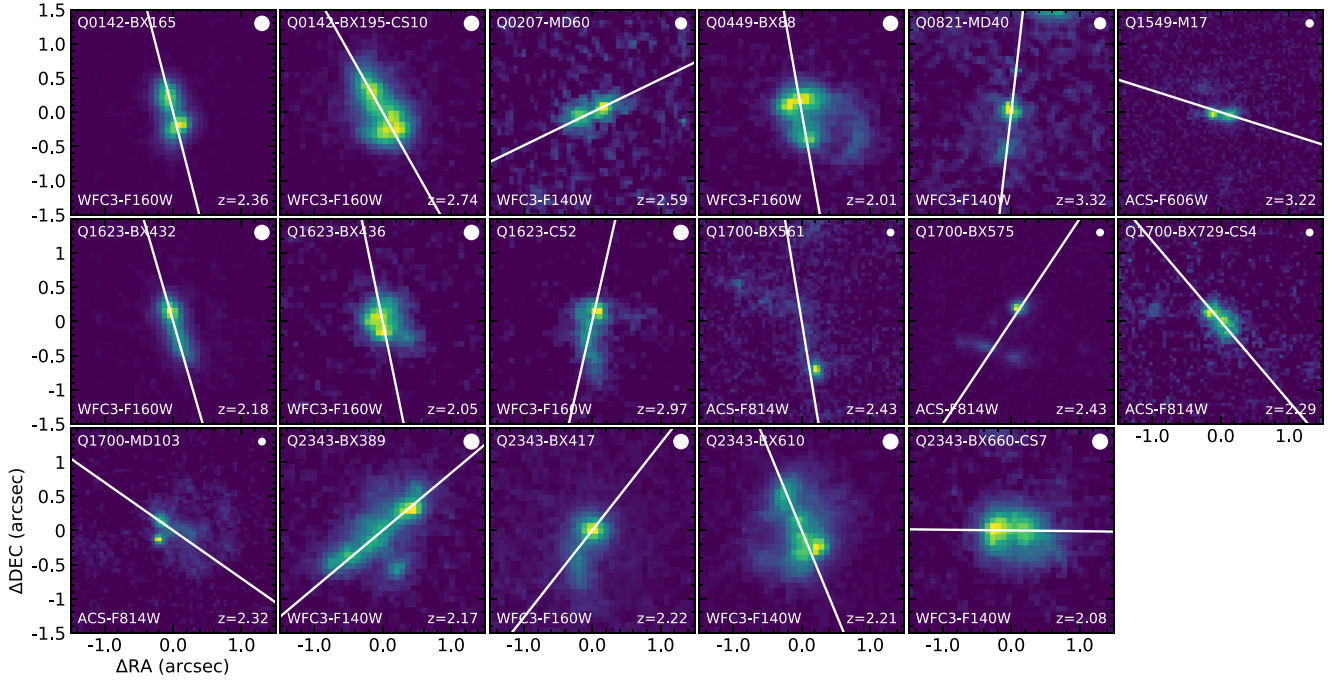
Figure 6. Same as Fig. 5, except that the galaxies do not have a clear central SB peak. Therefore, their PA_0 were determined only from the pixel moment (white solid line).
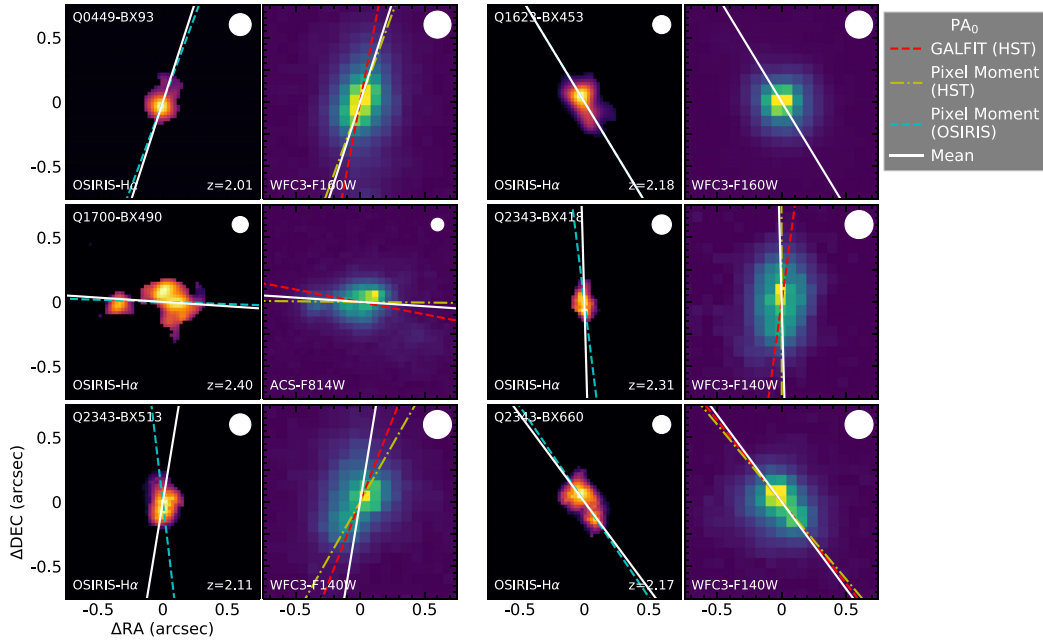
Figure 7. Similar to Fig. 5, showing the PA_0 of galaxies with both Keck/OSIRIS H α maps from Law et al. (2009) and *HST* continuum images. For each panel, the left image shows the OSIRIS H α map, in which the cyan dashed line is PA_0 measured from this map using second pixel moment. The right image shows the *HST* image, where the red dashed line and the yellow dash–dotted line show the PA_0 measured from GALFIT fitting and second moment from this image when present. The white solid lines are the final PA_0 determined for each galaxy by averaging the OSIRIS and *HST* measurements[8].

consistent with PA_0.[7] However, for Q2343-BX418, the implied PA_{kin}

is nearly perpendicular to its morphology-based PA_0. For Q1700-BX490, the kinematic structure is complicated by the presence of two distinct components: the brighter, western component appears to have $PA_{kin} \simeq 20$ degrees, which would be consistent with PA_0 measured from its H α intensity map; however, if the eastern component, which has a slightly blueshifted velocity of $\sim 100 km\ s^{-1}$,

[7]Q2343-BX513 was also observed by FS18, who found $PA_{kin} = -35$ degrees and $\Delta PA = 40 \pm 12$ degrees; our adopted $PA_0 = -9$ degrees differs by 26 degrees from their PA_{kin} value.
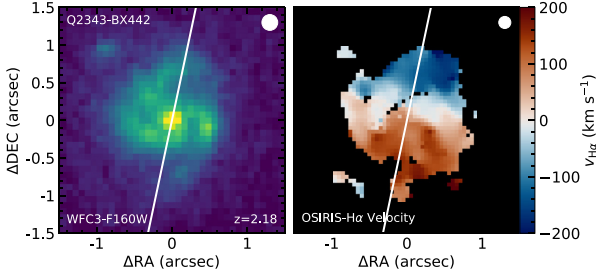
Figure 8. Left: *HST* WFC3-F160W image of Q2343-BX442. Right: Hα velocity map of Q2343-BX442 by Law et al. (2012a). The PA_0 (white solid line) is defined to be perpendicular to its rotational axis.
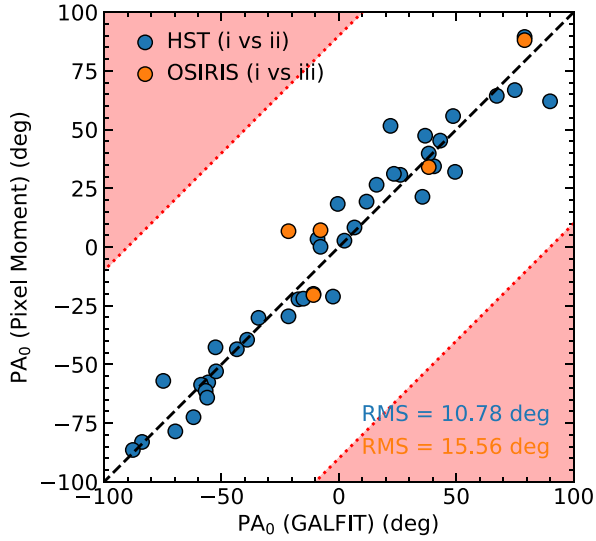
Figure 9. Comparison of PA_0 values measured using different methods. Blue points compare methods (i) and (ii), while orange points compare methods (i) and (iii). The red shaded regions indicate where the absolute differences between the two measurements are greater than 90 degrees, arithmetically forbidden because of the rotational symmetry. The overall rms =11.4 degrees.

is included as part of the same galaxy, we found $PA_0 = 86$ degrees.

As summarized in Table 1 and Figs 5–7, most of the galaxy sample has PA_0 measured using two or more of the methods described above, and generally the morphologically determined major axis PA_0 agrees with one another to within ~10 degrees. We caution that no high spatial-resolution *kinematic* information is available for most of the sample; based on the subset of nine that do have such measurements, approximately two-thirds show reasonable agreement between PA_0 and PA_{kin}.

4.4 Distribution and robustness of PA_0 measurements

To estimate the systematic uncertainty of the PA_0 measurements, we compare values measured using different methods for the same objects in Fig. 9. Between methods (i) and (ii), which are both based on *HST* images, the measured PA_0 for 40 galaxies are well centred along the 1:1 ratio, with rms $\simeq 10.8$ degrees. Values of PA0 measured using method (iii) are based on spectral line maps from an IFU rather than continuum light in a direct image, so that the 5 PA_0 values measured using methods (i) and (iii) exhibit larger scatter, with rms
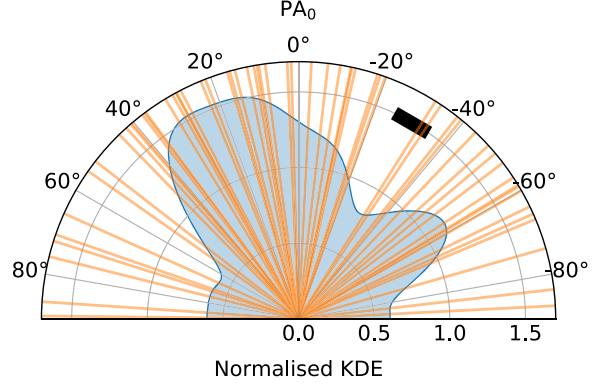
Figure 10. The kernel density estimate (KDE; blue shaded region) of PA_0 for the galaxy sample, normalized so that a uniform distribution would have a constant KDE = 1. The KDE was constructed using Gaussian kernels of fixed $\sigma = 10°$, corresponding to an opening angle represented by the black block at the top right. The orange solid lines indicate the values of PA_0 for the individual galaxies. There is an apparent excess in the KDE of galaxies with $PA_0 \simeq 10 - 40°$, which we attribute to sample variance.

$\simeq 15.6$ degrees relative to a 1:1 ratio. Therefore, we conclude that the uncertainty in final PA_0 measurements is $\lesssim 15$ degrees.

Fig. 10 shows the normalized kernel density estimator (KDE) and the individual measurements of PA_0. There is an apparent excess in the occurrence rate of values between $PA_0 \sim 10 - 40°$. To evaluate its possible significance, we conducted 1000 Monte Carlo realizations of a sample of 58 galaxies with randomly assigned PA_0; we find that there is an $\simeq 5$ per cent probability that a similar excess is caused by chance, thus is not statistically significant, and is consistent with that expected from sample variance.

Furthermore, because the *HST* and OSIRIS images used to measure PA_0 were rotated to the nominal North up and East left orientation prior to measurement, we tested whether significant bias might result from the choice of pixel grid by re-sampling all images with pixel grids oriented in five different directions. We found that the values measured for PA_0 were consistent to within 10 degrees (rms).

The possible systematic bias introduced by an uneven PA_0 distribution is mitigated by our observational strategy of rotating the KCWI instrument PA between individual exposures. We define PA_{Slicer} as the PA along the slices for each 1200-s exposure, and

$$\phi_{slicer} = |PA_{Slicer} - PA_0|. \tag{3}$$

Fig. 11(a) shows the distribution of ϕ_{slicer} in units of total exposure time. There is a slight tendency for the observations to align with the galaxy major axis (i.e. $\phi_{slicer} \sim 0$) that results from our usual practice of beginning a sequence of exposures of a given pointing with one at $PA_{slicer} = 0$ degree and the aforementioned excess of galaxies with $PA_0 \sim 20$ degrees.

In order to characterize the PSF of our final KCWI data cubes, and to show that it is effectively axisymmetric, Fig. 11(b) shows various composite images of the galaxy sample. Prior to forming the stack, each individual data cube was rotated to align the galaxy major (minor) axis with the X (Y) coordinate of the stacked image. The KCWI stacked galaxy continuum image [panel (i)] was made by integrating each aligned data cube along the wavelength axis over the range $1224 \leq \lambda_0/\text{Å} \leq 1236$ in the galaxy rest frame (i.e. $2000 < \Delta v/\text{km s}^{-1} \leq 5000$). This integration window was chosen to be representative of the UV continuum near Lyα without including the Lyα line itself and to be unaffected by Lyα absorption from the
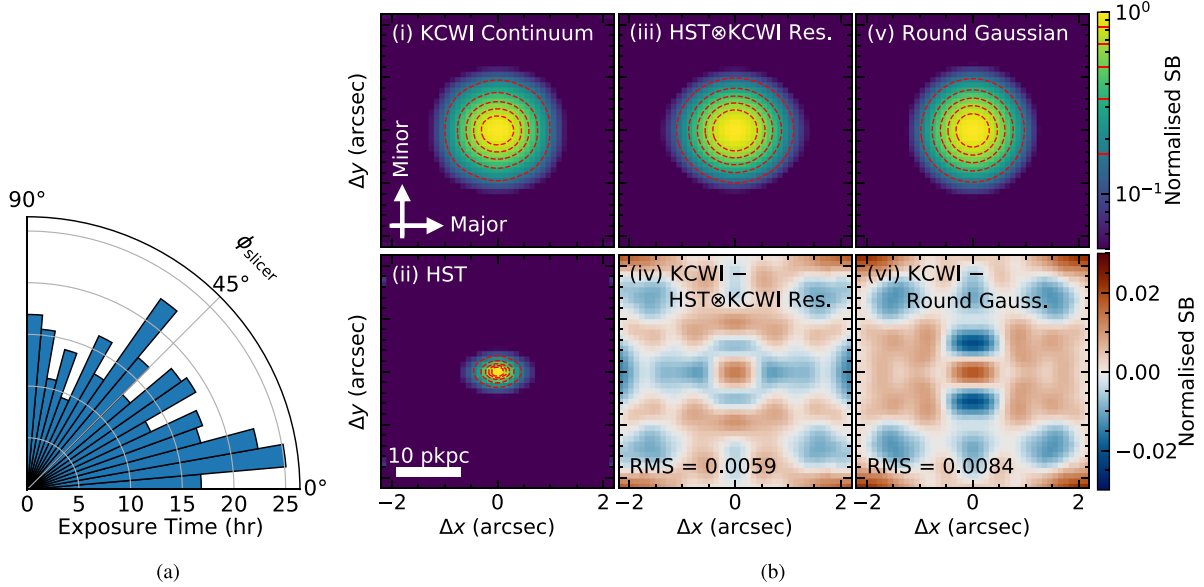
Figure 11. (a) Histogram of the relative contribution of measurements made at different slicer azimuthal angles (ϕ_{slicer}) in units of total exposure time. The distribution of ϕ_{Slicer} is relatively uniform, with a small excess near $\phi_{\text{Slicer}} \sim 10$ degrees. (b) Stacks of the galaxy continuum images for which the major and minor axes of each galaxy were aligned with the x- and y-axes prior to averaging. Each panel shows (i) the pseudo-narrow-band image (rest frame 1230 ± 6 Å) of the KCWI galaxy continuum, (ii) the stacked *HST* continuum image, after aligning the principal axes in the same way, (iii) the *HST* image convolved with a Gaussian kernel of FWHM = 1″.02 to match the KCWI continuum, (iv) the residual between the KCWI continuum and the *HST* image convolved with the KCWI PSF, (v) a 2D circular Gaussian profile with FWHM = 1.21 arcsec as the best symmetric Gaussian profile from a direct fit of the KCWI continuum image, and (vi) the residual between the KCWI continuum and the model in (v) isotropic Gaussian profile. The colour map of panels (i), (ii), (iii), and (v) is in log scale, with linear red contours in the decrement of 0.17. The colour map of panels (iv) and (vi) is in linear scale. The residual map in panel (vi) shows a clear dipole residual in the Y (minor axis) direction that is not present in panel (iv). The rms values in panels (iv) and (vi) were calculated within $|\Delta x| < 1$ arcsec and $|\Delta y| < 1$ arcsec to reflect the dipole residual. The 'boxiness' of the KCWI stack is likely due to the undersampling of KCWI in the spatial direction. Taken together, (b) demonstrates that the KCWI PSF is axisymmetric (with FWHM = 1″.02), and that the KCWI continuum image is capable of distinguishing the galaxy major and minor axes.
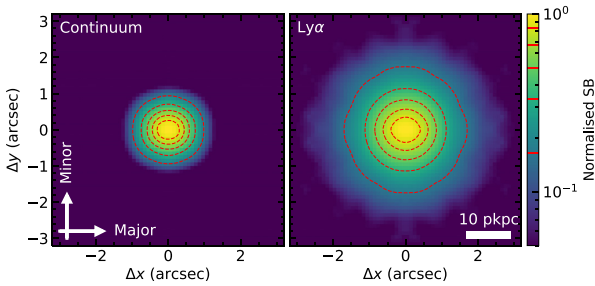
Figure 12. Stacked images of the galaxy continuum (Left) and the continuum-subtracted Lyα emission (Right) with the x- and y-axes aligned with the galaxy major and minor axes, respectively. The colour coding is on a log scale, while the contours are linear. The intensity scales have been normalized to have the same peak surface brightness intensity at the centre. The Lyα emission is more extended than the continuum emission.

IGM. The centre of the galaxy is determined with high confidence (see Section 5.1) by fitting a 2D Gaussian function to the individual galaxy continuum image. A similar approach – aligning the principal axes in the high-resolution *HST* images prior to stacking – was used to produce the *HST* stacked continuum image shown in panel (ii), except that the centres in the *HST* images were measured using the first moment of pixel intensity. Both stacks were conducted in units of observed SB. The FWHM of the stacked *HST* image along the major and minor axes are 0″.55 and 0″.35, respectively. The stacked KCWI continuum image is well reproduced by the convolution of

the PA$_0$-aligned stacked *HST* image [panel (ii) of Fig. 11(b)] with an axisymmetric 2D Gaussian profile with FWHM = 1″.02 [see panels (iii) and (iv) of Fig. 11(b)].

Comparing the convolution of *HST* and KCWI [panel (iii)] with the best direct fit of a symmetric Gaussian profile to the KCWI continuum image (FWHM = 1″.21) [panel (v)] shows that even at the $\simeq$1″.02 resolution of KCWI one can clearly distinguish the major axis elongation. The residual map assuming a symmetric Gaussian profile [panel (vi)] shows a clear dipole residual compared to panel (iv). Thus, Fig. 11 shows that (1) the PSF of the KCWI cubes is axisymmetric and thus has not introduced a bias to the azimuthal light distribution measurements and (2) the spatial resolution is sufficient to recognize non-axisymmetry even on sub-arcsec angular scales of the continuum light.

5 ANALYSES

5.1 Lyα spatial profile

To study the dependence of the Lyα emission profile on galaxy azimuthal angle, we first analyze the Lyα SB profile as a function of the impact parameter (or transverse distance, D_{tran}). Fig. 12 compares the stacked continuum and continuum-subtracted narrow-band Lyα emission, composed in the same way as in Fig. 11. The integration window of the Lyα image is $-700 < \Delta v/(\text{kms}^{-1}) \leq 1000$ (1213– 1220 Å) to include most of the Lyα emission (as shown later in Section 5.2). Continuum subtraction throughout this work was done spaxel-by-spaxel in the data cube of each target galaxy by subtracting
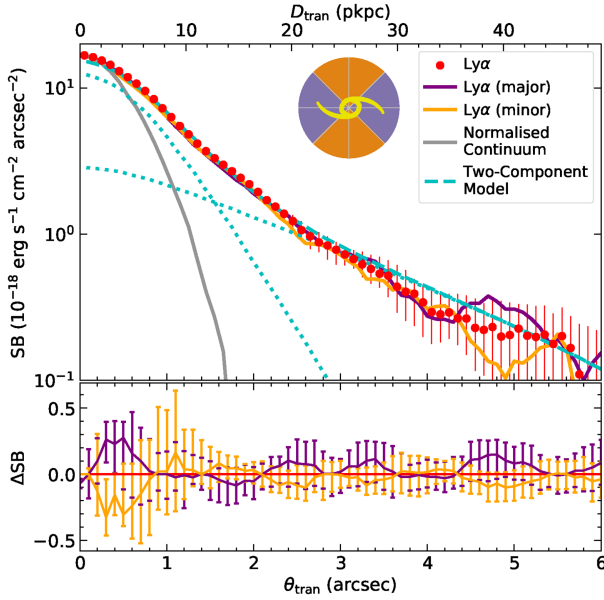
Figure 13. Top panel: The average Lyα surface brightness profile of the continuum-subtracted composite Lyα image shown in the right-hand panel of Fig. 12. Red points represent the median surface brightness evaluated over all azimuthal angles ($0° < \phi \leq 90°$) as a function of projected distance from the galaxy centre. Orange and purple curves show the profiles evaluated over $0° < \phi \leq 45°$ (major axis) and $45° < \phi < 90°$ (minor axis) azimuthal angles. Dashed cyan curve shows the best-fitting profile of the two-component exponential model. Dotted cyan curves show the two components separately. The grey profile shows the normalized continuum for comparison. Bottom: The residual surface brightness profile formed by subtracting the all-azimuth average from the major and minor axis profiles. The residuals are consistent with zero aside from a marginally significant difference at $\theta_{tran} < 1''.0$, where the Lyα emission is slightly stronger along the major axis. Unless otherwise noted, the conversion between θ_{tran} and D_{tran} for this and later figures assumes a redshift of 2.3, the median redshift of the sample.

the average flux density in two windows flanking the position of Lyα, with $2000 < |c\Delta v_{sys}/\mathrm{km\ s^{-1}}| < 5000$, where Δv_{sys} is the velocity separation relative to rest-frame Lyα (i.e. two windows each of width $\simeq 12$ Å in the rest frame [1195–1207] and [1224–1236] Å. Similar to Section 4.4, the centre of the galaxy in the KCWI data was determined by fitting a 2D Gaussian profile to the KCWI continuum image. The fitting box was chosen by eye to include all of the signal from the galaxy but excluding nearby contamination. Despite the arbitrary box size, we found that the derived centroid is very robust: varying the box size by 4 pixels (1''.2), the fit result does not change by more than 0''.01. The typical fitting error propagated from the reduced χ^2 is also ~0''.01 (median), i.e. much smaller than the seeing disc.

A 2D Gaussian fit to the profiles finds that the FWHM values are $1''.279 \pm 0''.003$ (major axis) $\times$ $1''.182 \pm 0''.003$ (minor axis) (or an ~ 8 per cent difference) for the continuum emission and $1''.689 \pm 0''.005 \times 1''.705 \pm 0''.005$ (< 1 per cent difference between major and minor axes) for the Lyα emission. Therefore, the Lyα emission in the stacked image is both more symmetric and more spatially extended than the continuum emission.

Fig. 13 shows the median Lyα SB as a function of D_{tran} (red). Each point represents the median SB of a bin of pixels with $\Delta D_{tran} = 0.1$ pkpc. The Lyα SB profile falls off much more slowly than the continuum (grey). Following Wisotzki et al. (2016), we fit the Lyα SB profile with a two-component model – a compact 'core' component

and an extended 'halo' component. Both components are exponential profiles convolved with the KCWI PSF with the amplitudes, exponential radii, and a uniform background term as free parameters. Further details of the model fitting will be described in a future work. The best-fitting exponential radii $r_{exp} = 3.71^{+0.06}_{-0.04}$ pkpc and $15.6^{+0.5}_{-0.4}$ pkpc. The r_{exp} of the halo component is close to Steidel et al. (2011) (for KBSS galaxies observed with narrow-band Lyα imaging), which found that the median-stacked Lyα profile has $r_{exp} = 17.5$ pkpc but slightly more extended than Wisotzki et al. (2018) for SF galaxies at $z > 3$ (see also Matsuda et al. 2012; Momose et al. 2014; Leclercq et al. 2017). Dividing the SB profiles into two subsamples with $0° \leq \phi < 45°$ (purple) and $45° \leq \phi \leq 90°$ (orange) that represent the galaxy major and major axes, respectively, one can see that the resulting profiles are consistent with one another to within 1σ, or within $\lesssim 2 \times 10^{-19}$ erg s^{-1} cm^{-2} arcsec^{-2}. The possible exception is at the smallest projected distances ($D_{tran} < 1$ arcsec, or $\lesssim 8$ pkpc), where the Lyα emission is marginally enhanced; if real, the difference in profiles (the asymmetry) represents < 2 per cent of the total Lyα flux. Thus, the composite Lyα intensity is remarkably symmetric, suggesting an overall lack of a strong statistical connection between the morphology of the starlight and that of the extended Lyα emission surrounding individual star-forming galaxies at $z \sim 2$–3.

5.2 Cylindrical projection of 2D spectra

The similarity of the Lyα SB profile along galaxy major and minor axes suggests that extended Lyα emission depends little on the galaxy orientation. However, the KCWI data cubes allow for potentially finer discrimination through examination of both the SB and the kinematics of Lyα emission as a function of projected galactocentric distance. To facilitate such comparison, we introduce 'cylindrical projections' of 2D Lyα emission. The basic idea behind cylindrical projection, illustrated in Fig. 14, is to provide an intuitive visualization of spatial and spectral information simultaneously.

Compared to the standard 2D spectrum one obtains from slit spectroscopy, the cylindrical 2D spectrum replaces the 1D spatial axis (i.e. distance along a slit) with projected distance by averaging spaxels in bins of D_{tran} or, equivalently, θ_{tran}. When projected as in the right-hand panel of Fig. 14, it can also be viewed as the Lyα spectrum at every projected radial distance (averaged, in this case, over all azimuthal angles) or as the average radial profile at each slice of wavelength or velocity.

Fig. 14 shows the stacked cylindrical 2D spectrum formed by averaging the continuum subtracted data cubes at wavelengths near rest-frame Lyα for all 59 galaxies in Table 1. This composite cylindrical 2D spectrum, analogous to a 'down-the-barrel' Lyα spectrum in 1D, but evaluated as a function of galactocentric distance, shows that the Lyα emission line comprises distinct redshifted and blueshifted components extending to ± 1000 km s^{-1} with respect to $v_{sys} = 0$, with a minimum close to $v_{sys} = 0$. The vast majority of individual galaxies, and therefore also the average in the stacked profile, has $F_{Ly\alpha}$(blue)/$F_{Ly\alpha}$(red) $\simeq 0.3$ and is thus 'red peak dominated'. The two-component spectral morphology extends to at least $\theta_{tran} \simeq 3$ arcsec or $D_{tran} \simeq 25$ pkpc. This overall spectral morphology is most readily explained as Lyα photons being resonantly scattered by outflowing material, whereby redshifted photons scattered from the receding (opposite) side are more likely to escape in the observer's direction than blueshifted photons (e.g. Pettini et al. 2001; Steidel et al. 2010; Dijkstra 2014).

As D_{tran} increases and the Lyα SB decreases exponentially, the two Lyα peaks become less distinct and merge into a symmetric 'halo' centred on $\Delta v = 0$. The vast majority of the Lyα emission is within
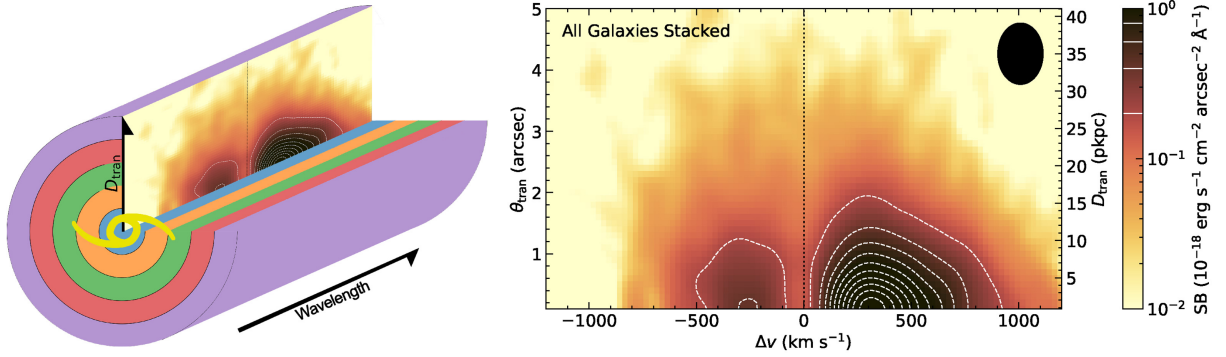
Figure 14. *Left*: A schematic diagram explaining cylindrically projected 2D (CP2D) spectra. Spaxels with similar D_{tran} are averaged to create the emission map in $D_{tran}-\Delta v$ space. *Right*: The composite CP2D spectra of the continuum-subtracted Lyα emission line map averaged over all 59 galaxies at all azimuthal angles (ϕ). The colour-coding of the Lyα surface intensity is on a log scale to show the full extent of the emission, whereas the contours are spaced linearly and marked as white lines in the colour bar. The stack was formed by shifting the wavelengths of each galaxy data cube to the rest frame, leaving the surface brightness in observed units. The black ellipse at the top right shows the effective resolution of the stacked maps, with principal axes corresponding to the spectral resolution FWHM and the spatial-resolution FWHM (see Section 4.4). Pixels with $\theta_{tran} < 0.1$ arcsec have been omitted to suppress artefacts owing to the singularity in the cylindrical projection.

$-700 < \Delta v/\mathrm{km\,s^{-1}} < 1000$. However, we caution that the apparent blue edge at $\Delta v \sim -700$ km s^{-1} of Lyα emission in this composite 2D spectrum is likely caused by continuum over-subtraction resulting from the relatively simple technique that we used in this work. The continuum subtraction assumed a linear interpolation of the continuum spectrum underneath the Lyα emission (see Section 5.1), which tends to over-estimate the continuum flux blueward of the systemic redshift of the galaxy due to intrinsic Lyα absorption in the stellar spectrum and residual effects of the often-strong Lyα absorption damping wings on which Lyα emission is superposed. To improve on this would require a more sophisticated continuum subtraction method in the inner $\simeq 1''.0$ of the galaxy profile; however, since most of the remainder of this work will involve comparison of 2D cylindrical projections with one another, the imperfections in continuum subtraction at small θ_{tran} are unlikely to affect the results.

5.3 Dependence on azimuthal angle of cylindrically projected 2D (CP2D) spectra

To investigate how Lyα emission depends on the galaxy azimuthal angle, we split each CP2D spectrum of individual galaxies averaged over two independent bins of azimuthal angle (ϕ) with respect to the galaxy's major axis: $0° \leq \phi < 45°$ ('major axis') and $45° \leq \phi \leq 90°$ ('minor axis'), as in Section 5.1 and Fig. 13. The CP2D stacks covering these azimuth ranges were combined separately to form CP2D composites that we refer to as 'major axis' and 'minor axis'. To reveal subtle differences in SB and/or velocity along these two directions, we subtracted one from the other – Fig. 15 shows the result.

The difference between the CP2D spectra along the major and minor axes (top right of Fig. 15) shows excess emission along the galaxy major axis at $\Delta v \simeq +300$ km s^{-1} – consistent with the velocity of the peak of the redshifted component in the full composite CP2D spectrum – within $\theta_{tran} \lesssim 2''$ ($D_{tran} \lesssim 15$ pkpc). The Lyα flux of this asymmetric component of Lyα amounts to $\lesssim 2$ per cent of the total and has a peak intensity $\simeq 5$ per cent that of the peak of the redshifted Lyα component shown in Fig. 13.

The significance map in the bottom right-hand panel of Fig. 15 is based on the standard deviation of 100 independent mock CP2D stacks, each made by assigning random PA$_0$ to the galaxies in

our sample before combining. The mock stacks were then used to produce a 2D map of the rms residuals evaluated in the same way as the observed data. Considering the effective resolution, the overall significance (compared to the standard deviation) of the most prominent feature in the top right-hand panel of Fig. 15 is $\simeq 2$–2.5σ per resolution element. Thus, while the residual (excess) feature may be marginally significant statistically, the level of asymmetry relative to the total Lyα flux is in fact very small.

5.4 The robustness of residual Lyα asymmetry

Despite the marginally significant detection of the excess Lyα emission along galaxy major axes, its robustness is subject to scrutiny. In particular, we would like to determine whether the apparent detection is typical of the population or is caused by a few outlier objects having very asymmetric Lyα as a function of azimuthal angle.

Fig. 16 shows histograms of the difference in integrated Lyα flux between the major and minor axis bins of azimuthal angle. We calculated the differences integrated over two different ranges of Δv and θ_{tran}; (1) the range where the excess shown in Fig. 15 is most prominent, $\theta_{tran} \leq 2''$ and $0 \leq (\Delta v)/\mathrm{km\,s^{-1}} \leq 500$, shown in the top panel, and (2) the range that encapsulates most of the redshifted component of Lyα $\theta_{tran} \leq 3''$ and $0 \leq (\Delta v)/\mathrm{km\,s^{-1}} \leq 1000$, shown in the bottom panel. Two galaxies – Q0142-BX165 and Q2343-BX418 – are clearly outliers in (1), while only Q0142-BX165 stands out in (2). The distribution of $\Delta F_{Ly\alpha}$ for the other 56 galaxies in the sample is relatively symmetric around $\Delta F_{Ly\alpha} = 0$.

Figs 17 and 18 show the stacked Lyα profiles as in Fig. 15 but with the strongest outliers removed from the stack. After removing both outliers (Fig. 18), the excess Lyα emission along the galaxy major axis at $\Delta v \simeq 300$ km s^{-1} becomes consistent with noise. Although Q2343-BX418 is not an extreme outlier in terms of the overall Lyα asymmetry of the integrated redshifted component of Lyα emission (bottom panel of Fig. 16), when only Q0142-BX165 is removed from the stack (Fig. 17), the composite 2D spectra still show obvious excess Lyα emission along the galaxy major axis, albeit with slightly reduced significance. Meanwhile, when both outliers are removed from the stack (Fig. 18), one can see an emerging excess Lyα emission along the *minor* axis, for the *blue* peak, with $-700 \lesssim \Delta v/(\mathrm{km\,s^{-1}}) \lesssim -200$ and $\theta_{tran} \lesssim 2''.5$ with integrated significance $\sim 2\sigma$. The flux of the excess blueshifted
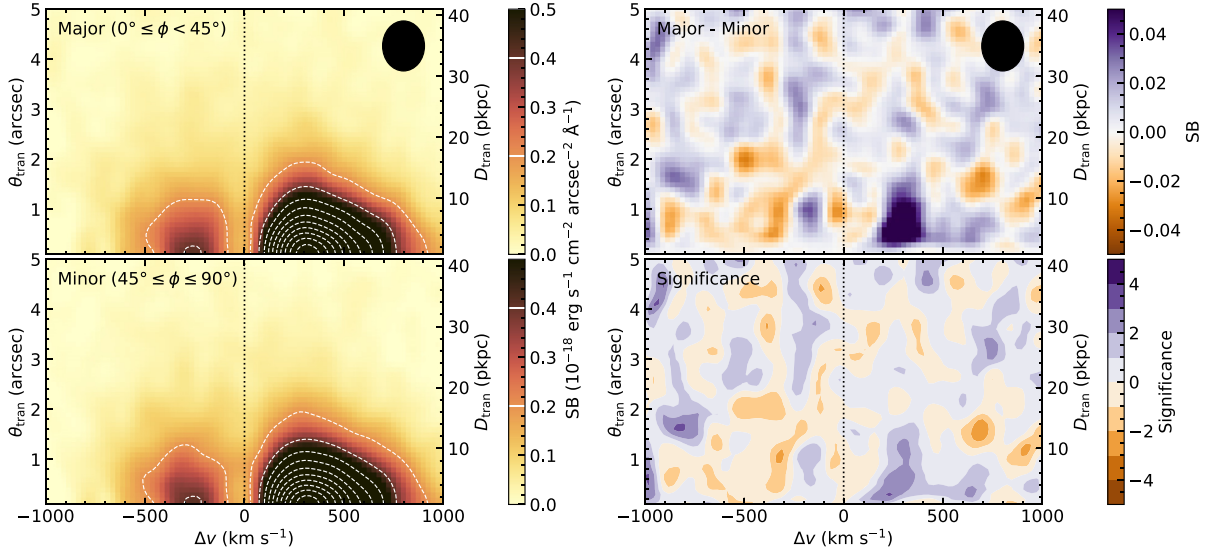
Figure 15. *Left*: The stacked CP2D spectra along the galaxy major ($0° \leq \phi < 45°$; top) and minor ($45° \leq \phi \leq 90°$; bottom) axes. Both the colour-coding and the contours are on linear scales. *Right*: The residual CP2D maps: the top panel shows the difference between the major axis and minor axis maps, in the same units of surface intensity as in the left-hand panels, where blue colours indicate regions with excess Lyα surface intensity along the major axis; orange colours indicate regions where Lyα is brighter in the minor axis map. The bottom panel shows the same residual map in units of the local noise level. The most prominent feature is excess Lyα emission along the galaxy major axis relative to that along the minor axis), at $\Delta v \sim +300$ kms^{-1}, extending to $\theta_{tran} \sim 2\rlap{.}''0$ or $D_{tran} \sim 15$ pkpc.
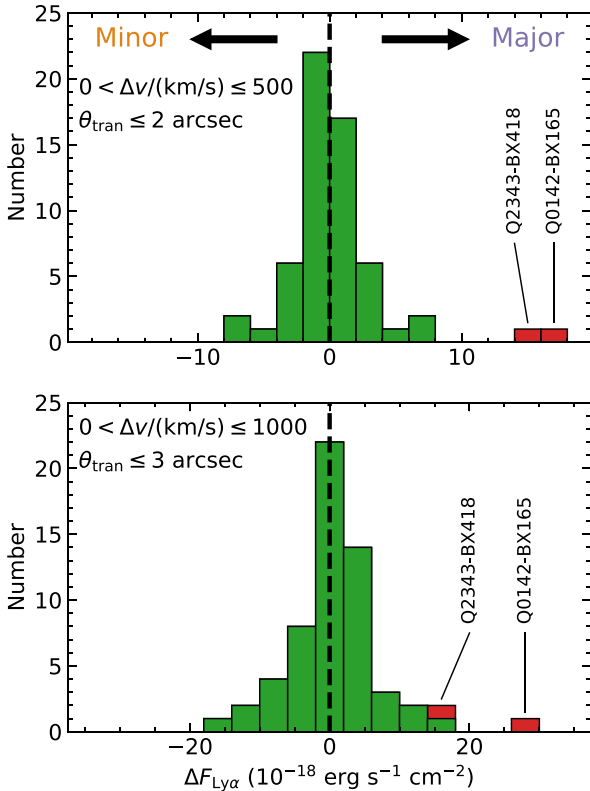
Figure 16. Distribution of the difference in Lyα flux integrated over velocity and angular distance in the bins of azimuthal angle corresponding to 'major' and 'minor' axes. Positive (negative) values indicate that Lyα emission is stronger along the major (minor) axis. The integration is conducted within $0 < \Delta v/(\mathrm{km\,s^{-1}}) < 500$ and $\theta_{tran} \leq 2$ arcsec (top) and $0 < \Delta v/(\mathrm{km\,s^{-1}}) < 1000$ and $\theta_{tran} \leq 3$ arcsec (bottom). There are two outliers in the first integration (top panel), while one remains in the second (bottom panel).

emission comprises $\sim$10 per cent of the total blueshifted Lyα flux, with a peak amplitude $\sim$1 per cent of the peak Lyα intensity (i.e. the redshifted peak).

We conducted an analysis on the *blueshifted* emission similar to that done for the redshifted asymmetry, with results summarized in Fig. 19. There is no obvious outlier in the difference in integrated Lyα flux between the major and minor axis azimuth bins except for Q0142-BX165, for which the excess again favours the *major* axis (i.e. it is in the direction opposite to the apparent blueshifted asymmetry identified in Fig. 18). We also consecutively removed from the Lyα stack galaxies with extreme excess emission along the minor axis and found no sudden and significant changes in the composite spectra. Evidently, the blueshifted excess along the minor axis, while of about the same significance as the redshifted excess in the major axis direction, is a general property of the full sample rather than a result of a small number of outliers.

In summary, we found excess emission along the galaxy major axis for the redshifted component of Lyα near $\Delta v \simeq 300$ km s^{-1}. However, this particular excess emission appears to be caused by galaxy outliers with extreme emission along the major axis. After removing them from the composite CP2D spectra, we found excess emission along the galaxy minor axis for the blue peak within $-700 \lesssim \Delta v/(\mathrm{km\,s^{-1}}) \lesssim -200$ that is not apparently affected by the extreme scenarios. Both detections are not particularly significant at the $\sim$2σ level.

5.5 A closer look at the extreme cases

Fig. 20 shows the residual between the cylindrically projected 2D spectra extracted along the major and minor axes of Q0142-BX165, as well as continuum images from both *HST* and KCWI. Q0142-BX165 has two comparably bright components separated by $\simeq 3.5$ pkpc ($\simeq 0\rlap{.}''4$). Careful inspection of Keck/LRIS and Keck/MOSFIRE spectra of this system revealed no sign of an object at a different redshift. There is no significant offset between
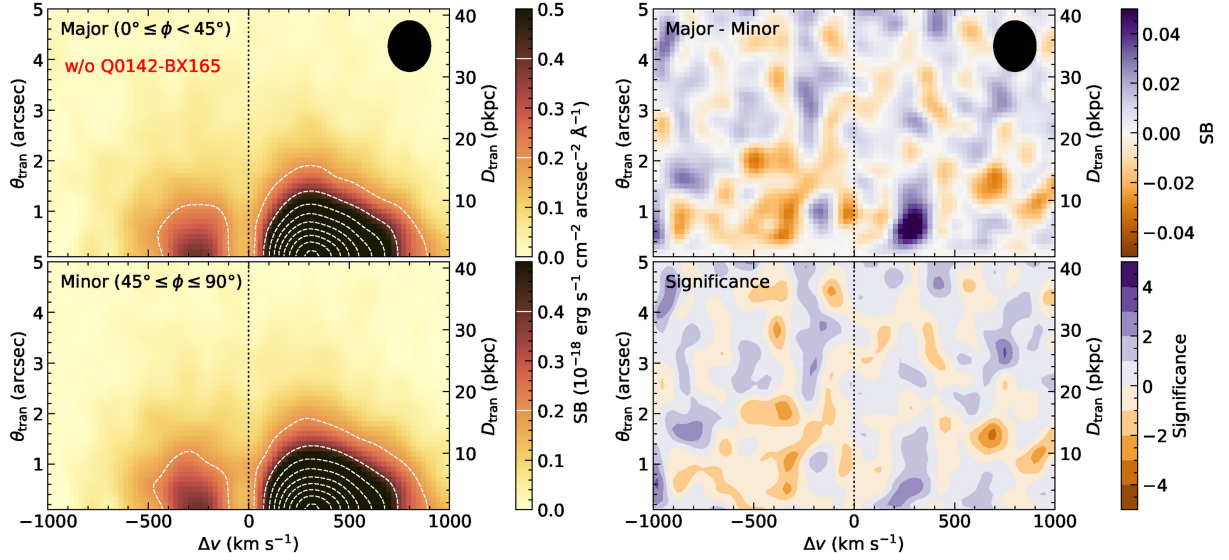
Figure 17. Same as Fig. 15, but without Q0142-BX165, which is the strongest outlier in terms of excess Lyα emission along the galaxy major axis.
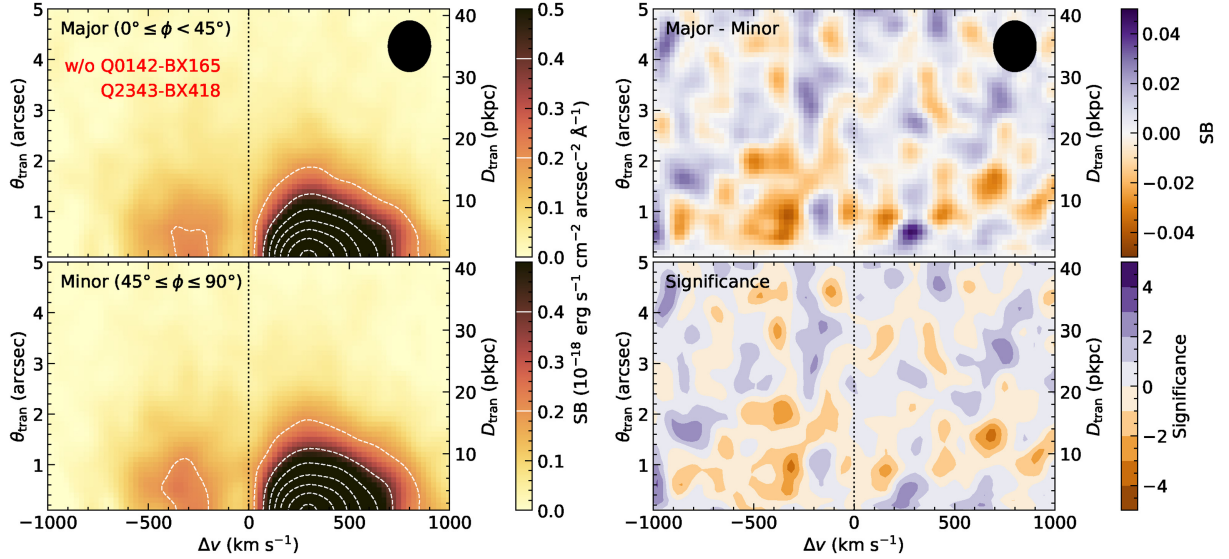

Figure 18. Same as Fig. 15, but without Q0142-BX165 and Q2343-BX418, the two most significant outliers in the top panel of Fig. 16. Significant excess emission that is larger than a resolution element for the redshifted peak no longer exists.

the KCWI continuum and the Lyα centroids (≤ 0.5 pix $\sim 0\overset{''}{.}15$ separation), indicating that the apparent directional asymmetry in the CP2D spectra is not caused by a spatial shift between the continuum and the Lyα emission. Instead, the narrow-band Lyα map shows that the Lyα emission is elongated approximately along the N–S direction. However, after aligning the KCWI and *HST* astrometry with reference to a nearby compact galaxy, we found that both the KCWI stellar continuum near Lyα and the narrow-band Lyα emission are centred near the SW component (see Fig. 20). It is possible that the SW component alone is responsible for the Lyα emission, in which case its PA_0 would be $-59°$, $\sim 70°$ off from what was determined in Section 4. However, adopting $PA_0 = -59°$ would cause BX165 to become an outlier with excess Lyα emission along the *minor* axis. Meanwhile, the elongation of the KCWI continuum aligns with the direction of the separation of the two components and is roughly consistent with the direction of the Lyα elongation as

well. This seems to suggest that the Lyα elongation simply reflects the asymmetry of the continuum source, albeit on a larger angular scale; however, as shown in Fig. 6, many galaxies in the sample possess similar morphologies, but Q0142-BX165 is the only one that shows extraordinary asymmetry in Lyα emission. In any case, Q0142-BX165 has a uniquely asymmetric Lyα halo, possibly due to source confusion. Consequently, we exclude it from most of the analysis that follows.

The KCWI data cube for Q2343-BX418 has been analyzed previously by Erb et al. (2018); here, we consider it in the context of the analysis of Q0142-BX165 above (see Fig. 21). The difference in peak SB between the major and minor axes CP2D spectra is nearly equal to that of Q0142-BX165 (2.4×10^{-18} erg s^{-1} cm^{-2} arcsec^{-2}Å^{-1} for both). However, the spatial extent of the excess emission is significantly smaller for Q2343-BX418. The *HST*/WFC3, KCWI continuum, KCWI Lyα images, and OSIRIS-Hα images all show
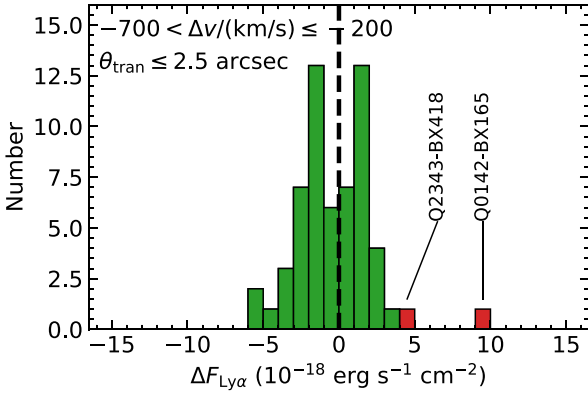
Figure 19. Same as Fig. 16, but with a different velocity range of $-700 < \Delta v/(\mathrm{km\,s^{-1}}) \leq -200$ and $\theta_{\mathrm{tran}} \leq 2.5$ arcsec that focuses on the blueshifted component of Lyα emission. No individual galaxy is an extreme outlier in terms of excess blueshifted Lyα along the minor axis.
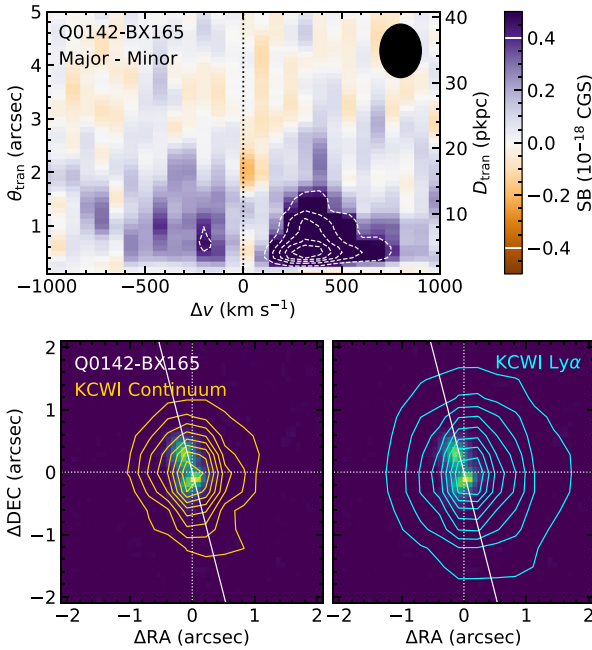

Figure 20. *Top*: Same as the top right-hand panel of Fig. 15, but for a single galaxy, Q0142-BX165, which has the strongest excess Lyα emission along the galaxy major axis. Note that the colour scale is 10 times that of Fig. 15. *Bottom*: The *HST* F160w image of Q0142-BX165, overlaid with contours from the KCWI continuum image (left) and the narrow-band Lyα image (right).

that Q2343-BX418 comprises a single component whose centroids in the various images are consistent with one another. Despite its extreme SB asymmetry in Lyα, Q2343-BX418 exhibits no other obviously peculiar property compared to the rest of the sample.

6 INTEGRATED LINE FLUX AND AZIMUTHAL ASYMMETRY

As shown in the previous sections, the degree of Lyα halo azimuthal asymmetry varies from case to case in our $z \simeq 2.3$ sample, but the correlation with the morphology of the central galaxy is sufficiently
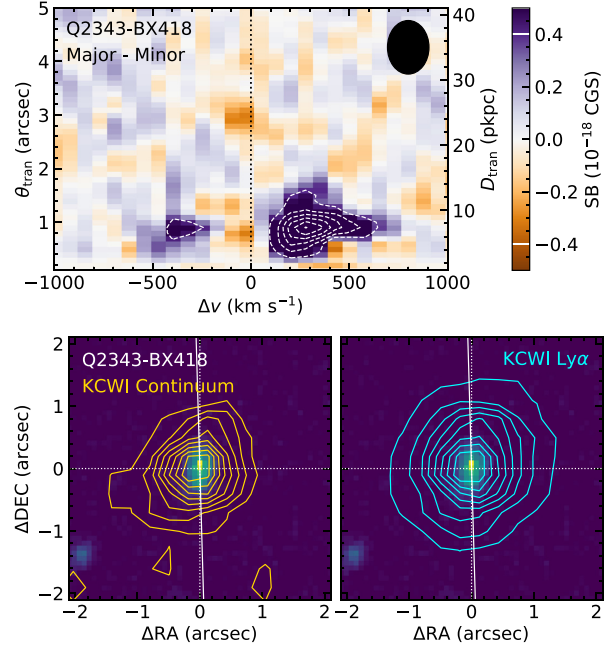

Figure 21. Same as Fig. 20 but for Q2343-BX418, the object with the second strongest major axis Lyα asymmetry.

weak that, on average, Lyα haloes are remarkably symmetric and appear to be nearly independent – both kinematically and spatially – of the apparent orientation of the galaxy at the centre.

Thus far, we have treated the blueshifted and redshifted components of Lyα emission separately. However, the overall Lyα profile is expected to provide clues to the geometry and velocity field of circumgalactic H I. In this section, we compare the dependency between excess Lyα emission and $W_\lambda(\mathrm{Ly}\alpha)$, total Ly$\alpha$ flux $F_{\mathrm{Ly}\alpha}(\mathrm{tot})$, and the ratio of the total flux of blueshifted and redshifted components of Lyα emission $[F_{\mathrm{Ly}\alpha}(\mathrm{blue})/F_{\mathrm{Ly}\alpha}(\mathrm{red})]$. The integration windows used to compute the values in Table 1 are $F_{\mathrm{Ly}\alpha}(\mathrm{tot})$: $\theta_{\mathrm{tran}} \leq 3$ arcsec and $-700 < \Delta v/(\mathrm{km\,s^{-1}}) \leq 1000$; $F_{\mathrm{Ly}\alpha}(\mathrm{blue})$: $\theta_{\mathrm{tran}} \leq 2.5$ arcsec and $-700 < \Delta v/(\mathrm{km\,s^{-1}}) \leq 0$; and $F_{\mathrm{Ly}\alpha}(\mathrm{red})$: $\theta_{\mathrm{tran}} \leq 3$ arcsec and $0 < \Delta v/(\mathrm{km\,s^{-1}}) \leq 1000$. Different integration windows were used for the two components in order to optimize the S/N of the integral; they were chosen based on the detected extent of each component in Fig. 17, in both θ_{tran} and Δv.

Fig. 22 examines whether or not there is a connection between major axis/minor axis asymmetry in Lyα flux and the overall Lyα halo properties mentioned above. For each pair of variables in Fig. 22, we indicate the value of the Pearson coefficient (r) and the corresponding probability p that the observed data set could be drawn from an uncorrelated parent sample. We also performed a linear regression using orthogonal distance regression in *SciPy*, which accounts for the estimated uncertainty in both x and y variables. As can be seen from the figure, most of the Pearson tests show no significant correlation and linear regression yields slopes consistent with zero. However, the Pearson test for the relation between $F_{\mathrm{major}}(\mathrm{blue}) - F_{\mathrm{minor}}(\mathrm{blue})$ and $F_{\mathrm{Ly}\alpha}(\mathrm{tot})$ (middle left-hand panel of Fig. 22) yields $p = 0.02$, suggesting a marginally significant trend in which the asymmetry of the blueshifted component of Lyα favours the minor axis when $F_{\mathrm{Ly}\alpha}(\mathrm{tot})$ is weak, and the major axis when $F_{\mathrm{Ly}\alpha}(\mathrm{tot})$ is strong.

The second relationship that stands out is $F_{\mathrm{major}}(\mathrm{red}) - F_{\mathrm{minor}}(\mathrm{red})$ and $F_{\mathrm{Ly}\alpha}(\mathrm{blue})/F_{\mathrm{Ly}\alpha}(\mathrm{red})$ (bottom right-hand panel of Fig. 22), where
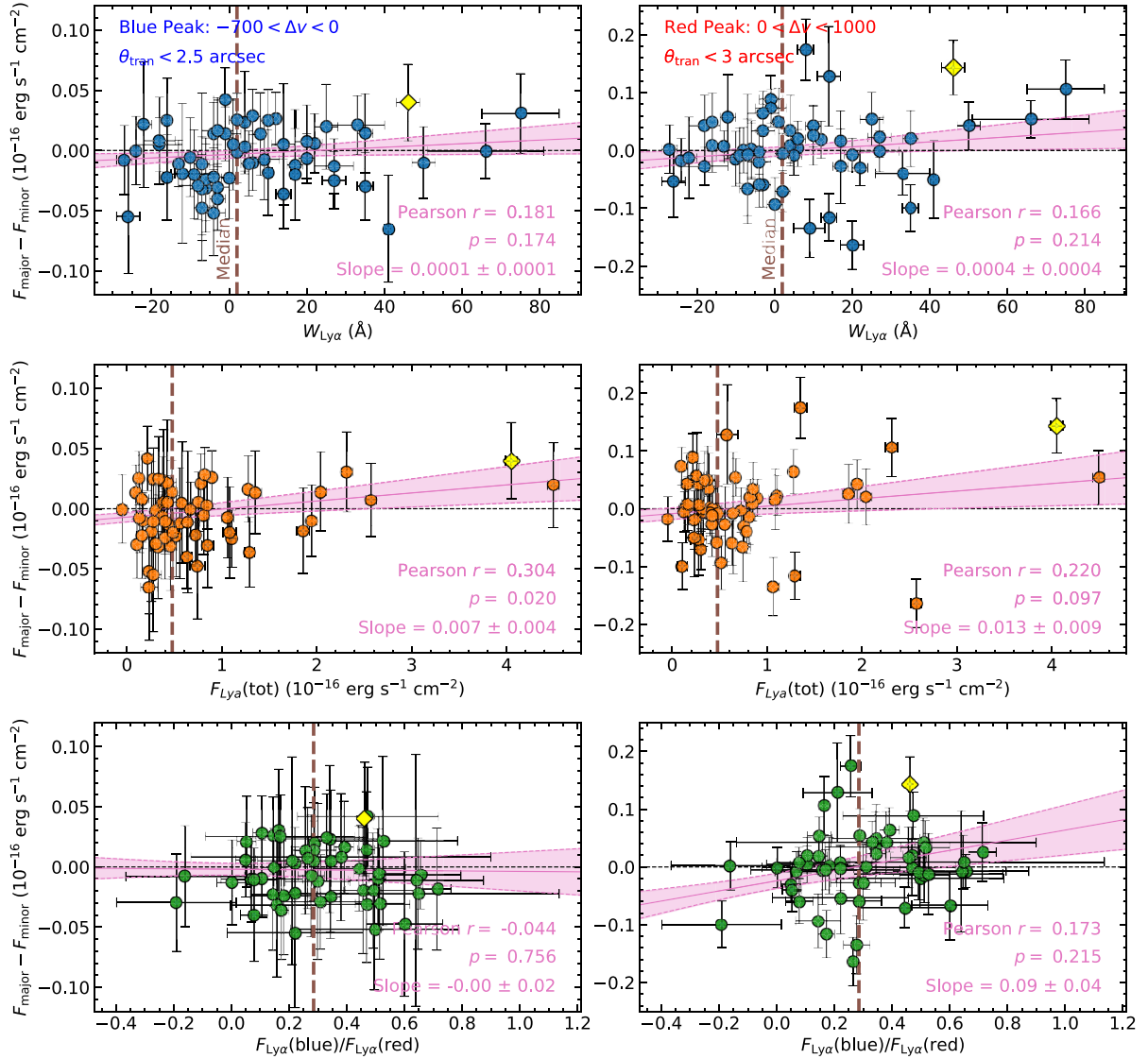
Figure 22. Relationship between the flux measurements of anisotropic (excess) Lyα emission ($\Delta F_{Ly\alpha} = F_{major} - F_{minor}$) of the blueshifted component (left) and redshifted component (right) of Lyα emission and properties of the integrated Lyα halo [*Top*: central Lyα equivalent width, $W_\lambda(Ly\alpha)$; *Middle*: total Lyα flux, $F_{Ly\alpha}(tot)$; *Bottom*: the ratio between the total blueshifted and redshifted components, $F_{Ly\alpha}(blue)/F_{Ly\alpha}(red)$]. Galaxies without reliable F_{red} are omitted in the bottom panel since their $F_{Ly\alpha}(blue)/F_{Ly\alpha}(red)$ are dominated by noise. The pink lines and shaded regions show the results and their 1σ uncertainties of a linear regression accounting for the errors in both x and y directions. The vertical dashed line in each panel marks the median value of the (x-axis) property for the full sample. The yellow diamond in each panel marks the location of Q2343-BX418, the outlier that caused the excess emission of the redshifted peak along the galaxy major axis as discussed in Section 5.5.

a non-parametric test for correlation is not significant. The linear regression results in a marginally significant positive slope, indicating that as the blueshifted component of Lyα approaches the strength of the redshifted component, there is a tendency for excess emission along the major axis; for galaxies with $F_{Ly\alpha}(blue)/F_{Ly\alpha}(red) \lesssim 0.3$ (i.e. smaller than the median value for the sample), the tendency is for excess Lyα emission along the minor axis.

To further explore the reliability of the correlations, we split the sample in two halves according to the overall halo properties and compared the subtracted CP2D spectra between the major and minor axes. Fig. 23 shows the result. As discussed in Section 5.5, the excess Lyα emission along the galaxy major axis for the red peak at $\Delta v \simeq 300$ km s^{-1} within $\theta_{tran} \lesssim 1$ arcsec can be attributed to a single outlier (Q2343-BX418), which happens to fall above the median

in all three quantities considered in Fig. 23 (i.e. on the right-hand panels of the figure). The subtracted CP2D spectra also indicate that essentially the entire excess Lyα emission for the blue peak along the minor axis – as identified earlier (Section 5.5) – is contributed by galaxies below the median $W_\lambda(Ly\alpha)$ and $F_{Ly\alpha}(tot)$ (top and middle left-hand panels of Fig. 23). In particular, the integrated significance within $-700 < \Delta v/(\text{km s}^{-1}) \leq -200$ and $\theta_{tran} \leq 2''.5$ exceeds 2.5σ for the $W_\lambda(Ly\alpha) <$ Median bin. Comparison of the top two panels also illustrates the same trend of $F_{major}(\text{blue}) - F_{minor}(\text{blue})$ versus $W_\lambda(Ly\alpha)$ and $F_{Ly\alpha}$ correlations suggested by Fig. 22.

For the subsamples divided based on the value of $F_{Ly\alpha}(\text{blue})/F_{Ly\alpha}(\text{red})$, the differences between the major axis and minor axis range of azimuthal angle are less significant: there is a marginally significant excess of Lyα emission, more noticeable in
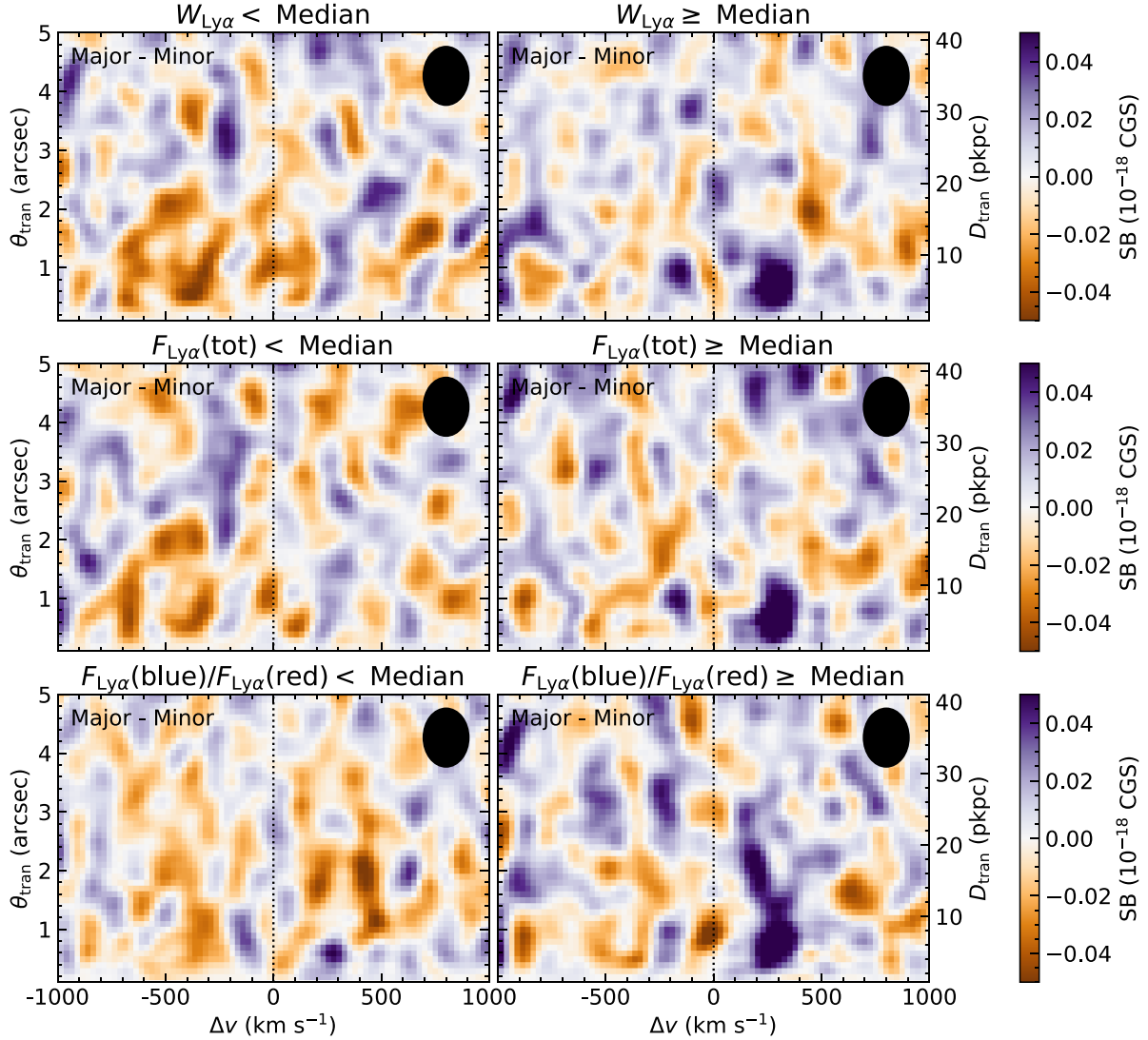
Figure 23. The difference between the CP2D spectra of Lyα emission for the major and minor axes. The maps show the residual for CP2D stacks for two sub-samples representing those below (left) and above (right) the sample median. From top to bottom, the Lyα halo properties are the central Lyα equivalent width ($W_\lambda(\text{Ly}\alpha)$), the integrated Lyα flux ($F_{\text{Ly}\alpha}(\text{tot})$), and the flux ratio between the blueshifted and redshifted components ($F_{\text{Ly}\alpha}(\text{blue})/F_{\text{Ly}\alpha}(\text{red})$). This figure confirms that the blueshifted excess Lyα emission favours weak Lyα-emitting galaxies.

the redshifted component, where it appears to extend over the range $\theta_{\text{tran}} \simeq 1-3$ arcsec, and the bin with higher $F_{\text{Ly}\alpha}(\text{blue})/F_{\text{Ly}\alpha}(\text{red})$ appears to have a major axis excess over approximately the same range of angular distances. If Q2343-BX418 is removed from the stack of larger $F_{\text{Ly}\alpha}(\text{blue})/F_{\text{Ly}\alpha}(\text{red})$ galaxies, the residual remains, showing that it is not attributable to a single outlier. However, none of the residuals in the bottom panels of Fig. 23 reaches a threshold of 2σ per resolution element.

In summary, a small statistical azimuthal asymmetry of Lyα haloes persists when the galaxy sample is divided into two according to central $W_\lambda(\text{Ly}\alpha)$, total $F_{\text{Ly}\alpha}$, and the flux ratio of blueshifted and redshifted emission. Perhaps most intriguing is that galaxies with small or negative central $W_\lambda(\text{Ly}\alpha)$ have a tendency to exhibit excess Lyα emission along galaxy minor axes extending over a fairly large range of both θ_{tran} and velocity ($-700 < (\Delta v/\text{km s}^{-1}) < -200$). The apparent excess along the major axis of redshifted Lyα for the subsample with stronger Lyα emission and larger $F_{\text{Ly}\alpha}(\text{blue})/F_{\text{Ly}\alpha}(\text{red})$, on the other hand, is confined to a smaller

range of (redshifted) velocities, again roughly coincident with the typical location of the 'red peak'.

7 FINER DIVISION OF GALAXY AZIMUTHAL ANGLES

At lower redshifts ($z < 1$), the covering fraction and column density of gas in various ionization stages are commonly found to be related to the orientation of the gaseous disc relative to the line of sight. Many authors have used background QSO or galaxy sightlines to detect strong Mg II absorbers associated with galaxies at redshifts to allow the foreground galaxy orientations to be measured (e.g. Steidel et al. 2002; Bordoloi et al. 2011; Bouché et al. 2012; Schroetter et al. 2019; Lundgren et al. 2021). A common conclusion is that the sightlines giving rise to strong absorption tend to be those located at azimuthal angles corresponding to both the galaxy major and minor axes, but fewer (strong) absorbers are found at intermediate angles, $30° < \phi < 60°$. The kinematics of the absorbing gas
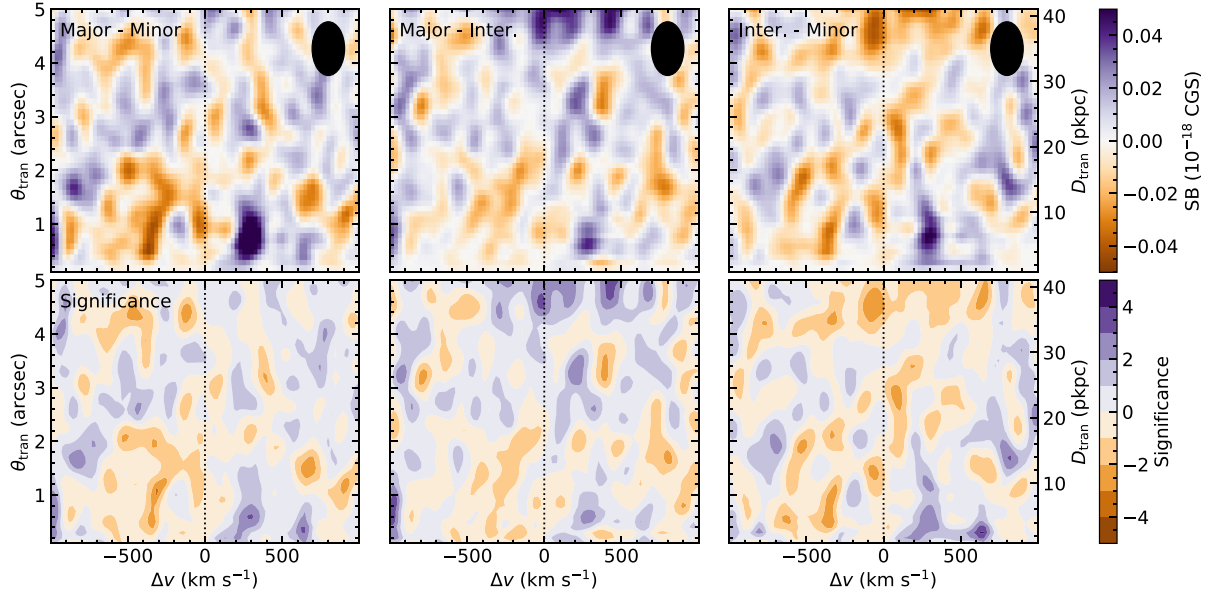
Figure 24. Similar to the right-hand panel of Fig. 15, but residual maps are between the major and minor (left), major and intermediate (middle), and intermediate and minor (right) axes with each bin size of only $\Delta\phi = 30°$. The strong residual beyond $\theta_{tran} > 4$ arcsec is caused by a contaminating source near a single object. No sign of a bimodal distribution of Lyα emission is present. The sample in this figure is the same as in Fig. 17 (Q0142-BX165: discarded; Q2343-BX418: included).

also appear to be related to ϕ (e.g. Ho et al. 2017; Martin et al. 2019), with the broadest (and therefore strongest) systems found along the minor axis, presumably due to fast bi-conical outflows oriented perpendicular to the disc, followed by major axis sightlines sampling accreting or galactic fountain gas sharing the halo's angular momentum and thus exhibiting disc-like rotation.

If the Lyα emission around $z = 2$–3 galaxies arises in CGM gas with properties similar to that of the low-ionization metallic absorbers at lower redshift, one might expect to see similar evidence for asymmetries along the two principal axes relative to intermediate azimuthal angles. We tested this possibility by expanding our analysis in Section 5.2 by dividing ϕ into three azimuthal bins – major axis ($0° \leq \phi < 30°$), minor axis ($60° \leq \phi \leq 90°$), and intermediate ($30° \leq \phi \leq 60°$). CP2D difference spectra among these three bins are shown in Fig. 24.

Fig. 24 shows no obvious sign of a bimodal distribution of Lyα emission with respect to ϕ, in which case the middle and right-hand panels would show residuals of opposite sign. Instead, the residual maps of 'Major−Intermediate' and 'Intermediate−Minor' suggest a gradual transition of the small asymmetries between major and minor axes in the larger bins of ϕ shown previously.

In any case, the main conclusion to draw from Fig. 24 is once again that Lyα emission haloes are remarkably similar in all directions with respect to the projected principal axes of $z \sim 2$–3 galaxies.

8 DISCUSSION

8.1 Comparison to previous work

The morphology of Lyα emission from the CGM and its relation to the host galaxies has been analyzed in various works between $z = 0$ and $z \lesssim 4$. However, analyses quantifying the Lyα emission with respect to the host galaxy orientation are limited. In this section, we attempt to compare the existing research on Lyα halo morphology with our findings.

At very low redshifts ($z = 0.02$–0.2), Guaita et al. (2015) studied the Lyα haloes of 14 Lyα-emitting galaxies in the Lyman Alpha Reference Sample (LARS; Östlin et al. 2014) and their connection to the host galaxy morphologies. They found that the Lyα haloes for the subset of the sample that would be considered Lyα emitters (LAE) are largely axisymmetric, and there is no single-galaxy morphological property that can be easily connected to the overall shape of the Lyα-emitting regions. Indeed, the Lyα images of the individual galaxies in Hayes et al. (2014) appear to be independent of galaxy orientation beyond $D_{tran} \sim 2$ pkpc. Meanwhile, the stacked Lyα image of the LARS galaxies is elongated in the same direction as the far-UV continuum, i.e. along the major axis. However, this stack could be significantly affected by sample variance from galaxies that are particularly bright in rest-UV and Lyα, as we saw for the KBSS sample before removing outliers. Interestingly, Duval et al. (2016) studied a special galaxy in the LARS sample, which is almost perfectly edge-on – they found two small Lyα-emitting components (each of extent <1 pkpc) near the disc consistent with Lyα emission escaping from the ISM through 'holes' in the galactic disc, akin to that expected in a classical Galactic fountain (Bregman 1980). While this is likely to be driven by stellar feedback allowing Lyα to escape in the direction perpendicular to the galaxy disc, the observed Lyα features are far closer to the galaxy than could be measured in our $z \sim 2$–3 sample. Moreover, most of the galaxies in our sample do not have organized thin discs and so likely have much lower dust column densities obscuring active star-forming regions.

At $z > 3$, Bacon et al. (2017) (and subsequent papers from the same group) conducted a systematic survey of Lyα-emitting galaxies in the Hubble Ultra Deep Field using VLT/MUSE. For example, Leclercq et al. (2017) found significant variation of Lyα halo morphology among 145 galaxies and identified correlations between the halo size and the size and brightness of the galaxy UV continuum. However, its connection with the galaxy morphological orientation remains to be investigated.

Meanwhile, Chen et al. (2020a) examined a case of a strongly lensed pair of galaxies with extended Lyα emission at $z > 3$. The

continuum image in the reconstructed source plane of their system A has at least three subcomponents extending over >1 arcsec, which may be similar to the subsample of galaxies shown in our Fig. 6, in terms of morphological complexity. In the context of the analysis we describe in the present work, this arrangement of Lyα with respect to continuum emission would be classified as excess minor axis Lyα emission. Unfortunately, the Lyα halo of a second $z > 3$ system is truncated in the source plane reconstruction.

In summary, we compared our result with galaxies and their Lyα emission morphology at $z \sim 0$ and $z > 3$ in previous work, finding that although our results are qualitatively consistent with earlier results, the comparison is hampered by limited sample sizes, as well as by differences in redshift and intrinsic galaxy properties represented in each sample.

8.2 Theoretical predictions

Many existing studies of the distribution and kinematics of CGM gas have focused on simulated galaxies within cosmological hydrodynamic simulations. Péroux et al. (2020) analyzed how inflowing and outflowing gas might distribute differently as a function of the galactic azimuthal angle within the EAGLE and IllustrisTNG simulations, finding significant angular dependence of the flow rate and direction, as well as the CGM metallicity, with outflows of higher metallicity gas favouring the galaxy minor axis, and accretion of more metal-poor gas tending to occur along the major axis at $z < 1$. Although Péroux et al. (2020) focused on $z \sim 0.5$ for their study, they made clear that the predicted trends would weaken significantly with increasing redshift.

At much higher redshifts ($z = 5$–7) around galaxies in the FIRE suite of simulations, Smith et al. (2019) found that Lyα escape is highly correlated with the direction of the H I outflow. Naively, one might expect that more Lyα would be found along the galaxy minor axis, which is the direction along which gaseous outflows would encounter the least resistance to propagation to large galactocentric radii. However, the galaxies experiencing the most active star formation at these redshifts tend to be altered on short time-scales ($\sim 10^7$ yr) by episodic accretion, star formation, and feedback events. Thus, the direction of outflows may change on similar time-scales, while the CGM will evolve on a longer time-scale, possibly erasing any clear signatures of alignment of outflows and Lyα emission. For the same reason, rapidly star-forming galaxies at $z \sim 2$–3, most of which have not yet established stable stellar discs, are likely to be surrounded by gas that is similarly turbulent and disordered.

Meanwhile, analytic or semi-analytic models of Lyα resonant scattering for idealized outflow geometries have focused primarily on the integrated Lyα emission profile from the entire galaxy or Lyα halo. Although many models account for the impact of the geometry and kinematics of gaseous outflows or accretion on the integrated Lyα emission profiles, there have been fewer efforts to predict the 2D spatial and spectral profiles for detailed comparison to IFU observations.

For example, Carr et al. (2018) constructed a model to predict the Lyα spectral morphology assuming bi-conical H I outflows with resonant scattering. The model predicts the integrated spectral profile without spatial information. In the context of the bi-conical outflow model, an integrated profile resembling our observation is predicted when the minor axis is perpendicular to the line of sight, with a large outflow having a small opening angle. However, this particular configuration would likely give rise to a highly asymmetric *spatial*

distribution of Lyα emission, which we have shown is unlikely to be consistent with our observations.

Our results highlight the need for 3D models of the cool gas in the CGM around rapidly star-forming galaxies at high redshifts, prior to the development of stable disc configuration, for which the assumption of axisymmetry of outflows, at least on average, may be closer to reality. In any case, predicting the spatial and spectral properties of Lyα *emission* will require realistic treatment of the kinematics, small-scale structure, and radiative transfer of Lyα photons from the sites of production to their escape last scattering from the CGM towards an observer.

Gronke et al. (2016) have devised a model that assumes a two-phase CGM, composed of optically thick clumps embedded in a highly ionized diffuse 'inter-clump' medium. This method has been used to fit the Lyα profiles at multiple locations within a spatially resolved 'Lyα blob' at $z \simeq 3.1$ (LAB) (Li et al. 2020). More recently, Li et al. 2021, have shown that the clumpy outflow models can be applied successfully to fit multiple regions within a spatially resolved Lyα halo simultaneously, i.e. using a central source producing Lyα which then propagates through a clumpy medium with an axisymmetric outflow (see also Steidel et al. 2011, who showed that Lyα emission haloes similar in extent to those presented in this paper are predicted naturally, given the observed velocity fields of outflows viewed DTB to the galaxy centre and the same radial dependence of clump covering fraction inferred from absorption line studies of background objects).

8.3 Implications for H I kinematics and Lyα radiative transfer

A spectral profile with a dominant redshifted component of Lyα emission line and a weaker blueshifted component – with peaks shifted by similar $|\Delta v|$ relative to the systemic redshift – is a typical signature of an expanding geometry, a central Lyα source function, and resonant scattering. It has also been shown that, for an ensemble of galaxies also drawn from the same KBSS redshift survey, the mean Lyα *absorption* signature measured in the spectra of background objects within $D_{tran} \lesssim 50$ pkpc ($\theta_{tran} \lesssim 6''$) is outflow-dominated (Chen et al. 2020b). However, although the observed Lyα haloes and their dependence on galaxy properties may be naturally explained by central Lyα sources scattering through the CGM, many authors have emphasized that collisionally excited Lyα emission from accreting gas (i.e. gravitational cooling – see e.g. Faucher-Giguère et al. 2010; Goerdt et al. 2010; Lake et al. 2015) and *in situ* photoionization by the UV background and/or local sources of ionizing photons (e.g. Leclercq et al. 2020) may also contribute significantly to extended Lyα haloes.

Due to the complex nature of Lyα radiative transfer, our results cannot resolve this issue definitively. However, the fact that the stacked CP2D Lyα spectra show asymmetry of <2 per cent between the major and minor axes for the ensemble, combined with (1) the empirical correlation between the central Lyα line strength (W_λ(Lyα)) and the Lyα flux integrated within the entire halo, and (2) the consistently red-peak-dominated kinematics of both the central and integrated Lyα line, all favour scattering of Lyα photons produced near the galaxy centre through an outflowing, clumpy medium – at least within $D_{tran} \lesssim 30$ pkpc. The remarkable statistical symmetry of the full 2D profiles, both spatially and spectrally, suggests that most of the galaxies in our sample lack persistent disc-like configurations, an inference supported also by the ubiquity of blueshifted absorption profiles in DTB spectra of similar galaxies and their lack of dependence on *HST* morphology (Law et al. 2012a, b). As a consequence, outflows do not behave in the manner expected for

central starbursts in disc galaxies; in other words, $z \sim 2$–3 galaxies on average appear to be more axisymmetric than their lower-redshift counterparts. This may have important implications for the cycling of gas and metals into and out of forming galaxies.

On the other hand, we have detected marginal (2σ) excess Lyα emission along the galaxy major axis for the red peak and along the galaxy minor axis for the blue peak. While most of the excess emission along the major axis can be easily explained by the relatively small sample size and the presence of one or two extreme cases, the excess blueshifted emission along the galaxy minor axis cannot be. While it is possible that the observed asymmetries indicate the prevalence of outflows along the major axis and inflows along the minor axis (i.e. the opposite of the behaviour of galaxies at $z <$ 1), we regard such an interpretation as unlikely. An important clue may be that most of the blueshifted, minor-axis excess is contributed by galaxies with weaker than the median Lyα emission strength – many in that subset have central $W_\lambda(\mathrm{Ly}\alpha) < 0$, meaning that Lyα photons must scatter from higher-velocity material or in directions with a more porous distribution of optically thick gas to have a high probability of escaping. Since we can observe only the photons that escape, galaxies with lower overall Lyα escape fractions will mean that those that do escape must take more extreme paths on average. As shown in Section 6, the galaxies with relatively weak emission also tend to have lower values of $F_{\mathrm{Ly}\alpha}(\mathrm{blue})/F_{\mathrm{Ly}\alpha}(\mathrm{red})$, which makes smaller absolute differences in emission strength versus azimuthal angle more noticeable.

Finally, we would like to emphasize the fact that the lack of a strong statistical correlation between the morphology of extended Lyα emission and the galaxy orientation does *not* imply that the individual Lyα haloes are symmetric. In fact, as shown in Figs 16, 19, and 22, individual Lyα haloes are often asymmetric, particularly for objects with weak central Lyα emission. Rather, our results indicate that morphological variations of Lyα haloes are uncorrelated with the apparent orientation of the host galaxy starlight.

9 SUMMARY

In this paper, we have presented the first statistical results of an IFU survey of star-forming galaxies at $\langle z \rangle = 2.43$ drawn from the KBSS and observed with the KCWI on the Keck 2 telescope. The 59 galaxies, with stellar mass and SFR typical of the full KBSS galaxy sample, comprise the subset of the KBSS–KCWI survey with both deep KCWI observations (typical exposure times of $\sim$5 h) and existing high spatial-resolution images from *HST* and/or Keck/OSIRIS. The high-resolution images were used to determine the direction of the projected major axis of the stellar continuum light of each galaxy; the KCWI IFU data cubes were used to detect spatially and spectrally resolved Lyα emission from the CGM around each galaxy to a limiting SB of $\lesssim 1 \times 10^{-19}$ ergs s^{-1} cm^{-2} arcsec^{-2} in the composite data (Fig. 13), enabling detection of diffuse Lyα emission haloes to projected distances of $\theta_{\mathrm{tran}} \simeq 4''$ ($D_{\mathrm{tran}} \simeq 30$ pkpc).

Our major findings are summarized below:

(i) We introduced 'cylindrically projected 2D spectra' (CP2D) in order to visualize and quantify Lyα spectra as a function of projected galactocentric distance D_{tran}. The CP2D spectra are averages of spaxels over a specified range of azimuthal angle (ϕ) at a common galactocentric distance, enabling statistical analyses of Lyα spectral profiles and their spatial variation simultaneously. The CP2D spectra clearly show distinct redshifted and blueshifted components of Lyα emission that remain distinct out to projected

distances of at least 25 pkpc, with rest-frame velocity extending from $-700 \le (\Delta v_{\mathrm{sys}}/\mathrm{km\ s}^{-1}) \lesssim 1000$ with respect to the galaxy systemic redshift, with blue and red peaks at $\simeq -300$ km s^{-1} and $\simeq +300$ km s^{-1}, respectively (Section 5.2).

(ii) We stacked the CP2D spectra of individual galaxies after aligning their continuum major axes in bins of azimuthal angle ϕ measured with respect to the major axis. By creating difference images of the CP2D projections in independent ranges of ϕ, we showed that residual differences between 'major axis' and 'minor axis' – which would reflect asymmetries in either the spatial or spectral dimension along different ranges of ϕ – are very small, with amplitude: $\lesssim 2 \times 10^{-20}$ erg s^{-1} cm^{-2} arcsec^{-2}Å^{-1}, corresponding to asymmetries in Lyα flux amounting to ≤ 2 per cent of the total, between galaxy major and minor axis directions (Section 5.3).

(iii) We found little evidence of statistically significant asymmetry of the Lyα emission, except for an excess ($\simeq 2\sigma$) of Lyα emission along galaxy major axes for the redshifted component of Lyα emission, with a peak near $\sim +300$ km s^{-1}. However, closer inspection revealed that most of the signal was caused by two galaxies with unusually asymmetric Lyα haloes. After discarding these outliers, another excess emission feature, with integrated significance $\simeq 2\sigma$, manifests as excess emission in the *blueshifted* component of Lyα along galaxy *minor* axes. This feature extends over a large range of velocity and appears to be contributed primarily by galaxies with weaker than the sample median Lyα emission and central Lyα equivalent width $W_\lambda(\mathrm{Ly}\alpha) < 0$. The same weak-Lyα subsample includes many of highest M_* galaxies in the sample, as well as many of the galaxies with the smallest flux ratio between blueshifted and redshifted components ($F_{\mathrm{Ly}\alpha}(\mathrm{blue})/F_{\mathrm{Ly}\alpha}(\mathrm{red})$). We speculate that this asymmetry may indicate that significant azimuthal variation of Lyα emission morphology exists only for galaxies with the smallest Lyα escape fractions within the sample, i.e. weaker Lyα-emitting galaxies possess more developed rotational structure. Evidently, one sees only the photons managing to find rare low-N_{HI} holes or that scatter from the highest velocity material, both of which are more likely along the minor axis (i.e. similar to expectations based on the standard picture of bi-conical starburst-driven outflows from disclike systems) (Sections 5.5 and 6).

(iv) Taken together, the results show that, statistically, the Lyα halo around galaxies in this sample (and, by extension, the population of relatively massive star-forming galaxies at $z \sim 2$–3) has remarkably little correlation – either kinematically or spatially – with the morphological distribution of stellar continuum light of the host galaxy. The observations suggest that most of the galaxies do not conform to expectations in which outflows are bi-conical and oriented along the minor axis of disc-like configurations, with accretion occurring preferentially along the major axis, suggested by observations of CGM gas in star-forming galaxies with $z < 1$. Instead, the lack of systematic variation in the kinematics and spatial extent with azimuthal angle of Lyα emission, together with the fact that $F_{\mathrm{Ly}\alpha}(\mathrm{blue})/F_{\mathrm{Ly}\alpha}(\mathrm{red})$ is universally smaller than unity, suggests that the bulk of Lyα at galactocentric distances $\lesssim 30$ pkpc is scattered from the inside out. The vast majority of scattered photons propagate through a scattering medium whose kinematics are dominated by outflows that are statistically symmetric with respect to the apparent morphology of a galaxy's starlight (Section 8).

This paper marks the first attempt to understand the relationship between Lyα emission in the CGM and its host galaxy properties in the KBSS–KCWI sample. As the central DTB Lyα emission was shown to be correlated with the host galaxy properties for the KBSS galaxies (e.g. Trainor et al. 2015, 2016, 2019), in forthcoming work,

we will utilize the CP2D spectra to further investigate the connection between the Lyα halo and observable properties of the host galaxies (e.g. stellar mass, SFR, SFR surface density, etc.) to understand whether galaxies at $z = 2$–3 significantly impact the H I distribution in the CGM and vice versa and to place additional constraints on the source functions and radiative transfer of Lyα in forming galaxies. With increased sample size and improved data reduction processes, we are also pushing to higher sensitivity in the stacked spectral cubes that allow us to probe the Lyα spectrum at larger galactocentric distances with high fidelity.

DATA AVAILABILITY

The composite CP2D spectra and the PYTHON program used to generate figures in this article are available upon reasonable request.

REFERENCES

Ao Y. et al., 2020, Nature Astron., 4, 670
Astropy Collaboration, 2018, AJ, 156, 123
Bacon R. et al., 2010, in McLean I. S., Ramsay S. K., Takami H., eds, Proc. SPIE Conf. Ser., Vol. 7735. Ground-based and Airborne Instrumentation for Astronomy III. SPIE, San Diego, California, United States, p. 773508
Bacon R. et al., 2017, A&A, 608, A1

Bordoloi R. et al., 2011, ApJ, 743, 10
Borisova E. et al., 2016, ApJ, 831, 39
Bouché N., Hohensee W., Vargas R., Kacprzak G. G., Martin C. L., Cooke J., Churchill C. W., 2012, MNRAS, 426, 801
Bregman J. N., 1980, ApJ, 236, 577
Bruzual G., Charlot S., 2003, MNRAS, 344, 1000
Byrohl C., Nelson D., Behrens C., Pillepich A., Hernquist L., Marinacci F., Vogelsberger M., 2020, MNRAS, 506, 5129
Cai Z. et al., 2019, ApJS, 245, 23
Calzetti D., Armus L., Bohlin R. C., Kinney A. L., Koornneef J., Storchi-Bergmann T., 2000, ApJ, 533, 682
Cantalupo S., Arrigoni-Battaia F., Prochaska J. X., Hennawi J. F., Madau P., 2014, Nature, 506, 63
Carr C., Scarlata C., Panagia N., Henry A., 2018, ApJ, 860, 143
Chabrier G., 2003, ApJ, 586, L133
Chen M. C., Chen H.-W., Gronke M., Rauch M., Broadhurst T., 2020a, MNRAS, 504, 2629
Chen Y. et al., 2020b, MNRAS, 499, 1721
Claeyssens A. et al., 2019, MNRAS, 489, 5022
Dijkstra M., 2014, PASA, 31, e040
Duval F. et al., 2016, A&A, 587, A77
Erb D. K., Steidel C. C., Chen Y., 2018, ApJ, 862, L10
Erb D. K., Steidel C. C., Shapley A. E., Pettini M., Adelberger K. L., 2004, ApJ, 612, 122
Faucher-Giguère C.-A., Kereš D., Dijkstra M., Hernquist L., Zaldarriaga M., 2010, ApJ, 725, 633
Förster Schreiber N. M. et al., 2009, ApJ, 706, 1364
Förster Schreiber N. M. et al., 2018, ApJS, 238, 21 (FS18)
Goerdt T., Dekel A., Sternberg A., Ceverino D., Teyssier R., Primack J. R., 2010, MNRAS, 407, 613
Gronke M., 2017, A&A, 608, A139
Gronke M., Dijkstra M., 2016, ApJ, 826, 14
Gronke M., Dijkstra M., McCourt M., Oh S. P., 2016, ApJ, 833, L26
Guaita L. et al., 2015, A&A, 576, A51
Harris C. R. et al., 2020, Nature, 585, 357
Hayes M. et al., 2014, ApJ, 782, 6
Ho S. H., Martin C. L., Kacprzak G. G., Churchill C. W., 2017, ApJ, 835, 267
Jones T., Stark D. P., Ellis R. S., 2012, ApJ, 751, 51
Kacprzak G. G., Churchill C. W., Evans J. L., Murphy M. T., Steidel C. C., 2011, MNRAS, 416, 3118
Kacprzak G. G., Churchill C. W., Nielsen N. M., 2012, ApJ, 760, L7
Kacprzak G. G., Muzahid S., Churchill C. W., Nielsen N. M., Charlton J. C., 2015, ApJ, 815, 22
Kakiichi K., Dijkstra M., 2018, MNRAS, 480, 5140
Kollmeier J. A., Zheng Z., Davé R., Gould A., Katz N., Miralda-Escudé J., Weinberg D. H., 2010, ApJ, 708, 1048
Kornei K. A., Shapley A. E., Erb D. K., Steidel C. C., Reddy N. A., Pettini M., Bogosavljević M., 2010, ApJ, 711, 693
Kulas K. R., Shapley A. E., Kollmeier J. A., Zheng Z., Steidel C. C., Hainline K. N., 2012, ApJ, 745, 33
Lake E., Zheng Z., Cen R., Sadoun R., Momose R., Ouchi M., 2015, ApJ, 806, 46
Lan T.-W., Mo H., 2018, ApJ, 866, 36
Larkin J. et al., 2006, Proc. SPIE, 6269, 62691A
Law D. R., Shapley A. E., Steidel C. C., Reddy N. A., Christensen C. R., Erb D. K., 2012a, Nature, 487, 338
Law D. R., Steidel C. C., Chen Y., Strom A. L., Rudie G. C., Trainor R. F., 2018, ApJ, 866, 119
Law D. R., Steidel C. C., Erb D. K., Larkin J. E., Pettini M., Shapley A. E., Wright S. A., 2007, ApJ, 669, 929
Law D. R., Steidel C. C., Erb D. K., Larkin J. E., Pettini M., Shapley A. E., Wright S. A., 2009, ApJ, 697, 2057
Law D. R., Steidel C. C., Shapley A. E., Nagy S. R., Reddy N. A., Erb D. K., 2012b, ApJ, 759, 29
Law D. R., Steidel C. C., Shapley A. E., Nagy S. R., Reddy N. A., Erb D. K., 2012c, ApJ, 745, 85
Leclercq F. et al., 2017, A&A, 608, A8

Leclercq F. et al., 2020, A&A, 635, A82

Li Z. et al., 2021, preprint (arXiv:2104.10682)

Li Z., Steidel C. C., Gronke M., Chen Y., 2020, MNRAS, 502, 2389

Lundgren B. F. et al., 2021, ApJ, 913, 50

Martin C. L., Ho S. H., Kacprzak G. G., Churchill C. W., 2019, ApJ, 878, 84

Martin D. C., Chang D., Matuszewski M., Morrissey P., Rahman S., Moore A., Steidel C. C., 2014, ApJ, 786, 106

Martin D. C., Matuszewski M., Morrissey P., Neill J. D., Moore A., Steidel C. C., Trainor R., 2016, ApJ, 824, L5

Matsuda Y. et al., 2012, MNRAS, 425, 878

Matthee J. et al., 2021, MNRAS, 505, 1382

McLean I. S. et al., 2012, in McLean I. S., Ramsay S. K., Takami H., eds, Proc. SPIE Conf. Ser., Vol. 8446. Ground-based and Airborne Instrumentation for Astronomy IV. SPIE, Amsterdam, Netherlands, p. 84460J

Momose R. et al., 2014, MNRAS, 442, 110

Morrissey P. et al., 2018, ApJ, 864, 93

Mostardi R. E., Shapley A. E., Steidel C. C., Trainor R. F., Reddy N. A., Siana B., 2015, ApJ, 810, 107

Nelson D. et al., 2019, MNRAS, 490, 3234

Nielsen N. M., Churchill C. W., Kacprzak G. G., Murphy M. T., Evans J. L., 2015, ApJ, 812, 83

O'Sullivan D. B., Martin C., Matuszewski M., Hoadley K., Hamden E., Neill J. D., Lin Z., Parihar P., 2020, ApJ, 894, 3

O'Sullivan D., Chen Y., 2020, preprint (arXiv:2011.05444)

Oke J. B. et al., 1995, PASP, 107, 375

Östlin G. et al., 2014, ApJ, 797, 11

Ouchi M., Ono Y., Shibuya T., 2020, ARA&A, 58, 617

Pahl A. J., Shapley A., Steidel C. C., Chen Y., Reddy N. A., 2021, MNRAS, 505, 2447

Partridge R. B., Peebles P. J. E., 1967, ApJ, 147, 868

Peng C. Y., Ho L. C., Impey C. D., Rix H.-W., 2002, AJ, 124, 266

Peng C. Y., Ho L. C., Impey C. D., Rix H.-W., 2010, AJ, 139, 2097

Péroux C., Nelson D., van de Voort F., Pillepich A., Marinacci F., Vogelsberger M., Hernquist L., 2020, MNRAS, 499, 2462

Peter A. H. G., Shapley A. E., Law D. R., Steidel C. C., Erb D. K., Reddy N. A., Pettini M., 2007, ApJ, 668, 23

Pettini M., Shapley A. E., Steidel C. C., Cuby J.-G., Dickinson M., Moorwood A. F. M., Adelberger K. L., Giavalisco M., 2001, ApJ, 554, 981

Reddy N. A., Steidel C. C., 2009, ApJ, 692, 778

Rudie G. C. et al., 2012, ApJ, 750, 67

Schroetter I. et al., 2019, MNRAS, 490, 4368

Sérsic J. L., 1963, Boletin de la Asociacion Argentina de Astronomia La Plata Argentina, 6, 41

Shapley A. E., Steidel C. C., Pettini M., Adelberger K. L., 2003, ApJ, 588, 65

Smith A., Ma X., Bromm V., Finkelstein S. L., Hopkins P. F., Faucher-Giguère C.-A., Kereš D., 2019, MNRAS, 484, 39

Song H., Seon K.-I., Hwang H. S., 2020, ApJ, 901, 41

Sravan N. et al., 2016, MNRAS, 463, 120

Stanway E. R., Eldridge J. J., 2018, MNRAS, 479, 75

Steidel C. C. et al., 2014, ApJ, 795, 165

Steidel C. C., Bogosavljević M., Shapley A. E., Kollmeier J. A., Reddy N. A., Erb D. K., Pettini M., 2011, ApJ, 736, 160

Steidel C. C., Bogosavljević M., Shapley A. E., Reddy N. A., Rudie G. C., Pettini M., Trainor R. F., Strom A. L., 2018, ApJ, 869, 123

Steidel C. C., Erb D. K., Shapley A. E., Pettini M., Reddy N., Bogosavljević M., Rudie G. C., Rakic O., 2010, ApJ, 717, 289

Steidel C. C., Kollmeier J. A., Shapley A. E., Churchill C. W., Dickinson M., Pettini M., 2002, ApJ, 570, 526

Steidel C. C., Shapley A. E., Pettini M., Adelberger K. L., Erb D. K., Reddy N. A., Hunt M. P., 2004, ApJ, 604, 534

Steidel C. C., Strom A. L., Pettini M., Rudie G. C., Reddy N. A., Trainor R. F., 2016, ApJ, 826, 159

Strom A. L., Steidel C. C., Rudie G. C., Trainor R. F., Pettini M., Reddy N. A., 2017, ApJ, 836, 164

Theios R. L., Steidel C. C., Strom A. L., Rudie G. C., Trainor R. F., Reddy N. A., 2019, ApJ, 871, 128

Trainor R. F., Steidel C. C., Strom A. L., Rudie G. C., 2015, ApJ, 809, 89

Trainor R. F., Strom A. L., Steidel C. C., Rudie G. C., 2016, ApJ, 832, 171

Trainor R. F., Strom A. L., Steidel C. C., Rudie G. C., Chen Y., Theios R. L., 2019, ApJ, 887, 85

Tumlinson J., Peeples M. S., Werk J. K., 2017, ARA&A, 55, 389

Vanzella E. et al., 2017, MNRAS, 465, 3803

Veilleux S., Cecil G., Bland-Hawthorn J., 2005, ARA&A, 43, 769

Verhamme A. et al., 2018, MNRAS, 478, L60

Verhamme A., Dubois Y., Blaizot J., Garel T., Bacon R., Devriendt J., Guiderdoni B., Slyz A., 2012, A&A, 546, A111

Verhamme A., Schaerer D., Maselli A., 2006, A&A, 460, 397

Virtanen P. et al., 2020, Nature Methods, 17, 261

Whitaker K. E. et al., 2014, ApJ, 795, 104

Wisotzki L. et al., 2016, A&A, 587, A98

Wisotzki L. et al., 2018, Nature, 562, 229

Zheng Z., Cen R., Trac H., Miralda-Escudé J., 2011, ApJ, 726, 38

This paper has been typeset from a TEX/LATEX file prepared by the author.